ELEMENTA
Science of the Anthropocene

Barten, JGM, et al. 2023. Low ozone dry deposition rates to sea ice during the MOSAiC field campaign: Implications for the Arctic boundary layer ozone budget. *Elem Sci Anth*, 11: 1. DOI: https://doi.org/10.1525/elementa.2022.00086

RESEARCH ARTICLE

Low ozone dry deposition rates to sea ice during the MOSAiC field campaign: Implications for the Arctic boundary layer ozone budget

Johannes G.M. Barten[1,*], Laurens N. Ganzeveld[1], Gert-Jan Steeneveld[1], Byron W. Blomquist[2,3], Hélène Angot[4,5], Stephen D. Archer[6], Ludovic Bariteau[2,3], Ivo Beck[4], Matthew Boyer[7], Peter von der Gathen[8], Detlev Helmig[5,9], Dean Howard[3,5], Jacques Hueber[5,10], Hans-Werner Jacobi[11], Tuija Jokinen[7,12], Tiia Laurila[7], Kevin M. Posman[6], Lauriane Quéléver[7], Julia Schmale[4], Matthew D. Shupe[2,3], and Maarten C. Krol[1,13]

Dry deposition to the surface is one of the main removal pathways of tropospheric ozone (O_3). We quantified for the first time the impact of O_3 deposition to the Arctic sea ice on the planetary boundary layer (PBL) O_3 concentration and budget using year-round flux and concentration observations from the Multidisciplinary drifting Observatory for the Study of Arctic Climate (MOSAiC) campaign and simulations with a single-column atmospheric chemistry and meteorological model (SCM). Based on eddy-covariance O_3 surface flux observations, we find a median surface resistance on the order of 20,000 s m^{-1}, resulting in a dry deposition velocity of approximately 0.005 cm s^{-1}. This surface resistance is up to an order of magnitude larger than traditionally used values in many atmospheric chemistry and transport models. The SCM is able to accurately represent the yearly cycle, with maxima above 40 ppb in the winter and minima around 15 ppb at the end of summer. However, the observed springtime ozone depletion events are not captured by the SCM. In winter, the modelled PBL O_3 budget is governed by dry deposition at the surface mostly compensated by downward turbulent transport of O_3 towards the surface. Advection, which is accounted for implicitly by nudging to reanalysis data, poses a substantial, mostly negative, contribution to the simulated PBL O_3 budget in summer. During episodes with low wind speed (<5 m s^{-1}) and shallow PBL (<50 m), the 7-day mean dry deposition removal rate can reach up to 1.0 ppb h^{-1}. Our study highlights the importance of an accurate description of dry deposition to Arctic sea ice in models to quantify the current and future O_3 sink in the Arctic, impacting the tropospheric O_3 budget, which has been modified in the last century largely due to anthropogenic activities.

Keywords: Ozone deposition, Arctic ozone, Modelling, Atmospheric boundary layer

1. Introduction

Tropospheric ozone (O_3) acts both as a greenhouse gas and air pollutant negatively affecting human health (Nuvolone et al., 2018) and plant growth (Ainsworth et al., 2012). Furthermore, O_3 plays an important role in atmospheric oxidation chemistry. On the global scale, the main O_3

[1] Meteorology and Air Quality Section, Wageningen University, Wageningen, the Netherlands
[2] NOAA Physical Sciences Laboratory, Boulder, CO, USA
[3] Cooperative Institute for Research in Environmental Sciences, University of Colorado, Boulder, CO, USA
[4] Extreme Environments Research Laboratory, École Polytechnique Fédérale de Lausanne Valais Wallis, Sion, Switzerland
[5] Institute for Arctic and Alpine Research, University of Colorado, Boulder, CO, USA
[6] Bigelow Laboratory for Ocean Sciences, East Boothbay, ME, USA
[7] Institute for Atmospheric and Earth System Research, INAR/Physics, University of Helsinki, Helsinki, Finland
[8] Alfred Wegener Institute, Helmholtz Centre for Polar and Marine Research, Potsdam, Germany
[9] Boulder AIR, Boulder, CO, USA
[10] JH Atmospheric Instrument Design, Boulder, CO, USA
[11] Institute for Geosciences and Environmental Research, CNRS/Université Grenoble Alpes/IRD/G-INP, Grenoble, France
[12] Climate & Atmosphere Research Centre (CARE-C), The Cyprus Institute, Nicosia, Cyprus
[13] Institute for Marine and Atmospheric Research Utrecht, Utrecht University, Utrecht, the Netherlands

* Corresponding author:
Email: sjoerd.barten@wur.nl

sources are photochemical production and stratosphere-troposphere exchange. Tropospheric O_3 is removed by dry deposition to the Earth's surface and by photochemical destruction (Lelieveld and Dentener, 2000). Due to its relatively short atmospheric lifetime (3 to 4 weeks) compared to other greenhouse gases, tropospheric O_3 is subject to high spatiotemporal variability, especially close to the Earth's surface. Many local processes determine the evolution of the O_3 concentration in the planetary boundary layer (PBL). These processes include local O_3 precursor emissions, dry deposition to the Earth's surface, advection of different air masses, vertical mixing in the PBL and entrainment of O_3-rich free tropospheric air as a result of PBL growth (Ganzeveld et al., 2008; Lin et al., 2009; Tang et al., 2017; Lu et al., 2019).

In the Arctic, tropospheric O_3 has been increasing up to the beginning of this century due to increasing emissions of precursors and long-range transport from the mid-latitudes (Cooper et al., 2014). During the last decades (2000 to 2020), the trend in Arctic tropospheric O_3 has been leveling off or even showing some decrease at individual sites (Cooper et al., 2020). Long-term O_3 observations at coastal sites such as Utqiagvik (Alaska, USA), Alert (Canada) and Zeppelin (Norway) have shown a clear seasonality in surface O_3 and a common occurrence of ozone depletion events (ODEs) in springtime. ODEs are often defined as events when the surface O_3 mixing ratio drops below 10 ppb and even down to almost 0 ppb (Simpson et al., 2007; Yang et al., 2020). These ODEs have been attributed to activation of reactive bromine chemistry in the PBL from sea-ice and snow-covered surfaces (Falk and Sinnhuber, 2018; Marelle et al., 2021; Swanson et al., 2022). Recently, Zhou et al. (2020) showed that the ODEs are also sensitive to the background nitrogen oxides (NO_x) concentrations. Local anthropogenic emissions of O_3 precursors are generally absent in the Arctic due to its remote location. Therefore, the O_3 PBL budget is predominantly driven by dry deposition to snow, ice (Helmig et al., 2007) and the Arctic Ocean (Barten et al., 2021), natural O_3 precursor emissions and halogen chemistry (Yang et al., 2020), atmospheric stability (Van Dam et al., 2016), and long-range transport of O_3 and its precursors.

Many previous studies have quantified the O_3 budget and controlling factors for (sub-)urban (Tang et al., 2017; Zhao et al., 2019), rural (Senff et al., 1996; Berkowitz et al., 2000; Hou et al., 2015), forested (Cros et al., 2000; Wolfe et al., 2011; Chen et al., 2018) or marine (Monks et al., 2000; Conley et al., 2011) environments. However, less effort has been spent to understand O_3 dynamics in- and above the Arctic PBL. Compared to the previously mentioned environments, the Arctic PBL is characterized by the occurrence of strong surface inversions (Tjernström et al., 2019), especially in autumn, winter, and spring (Zhang et al., 2011). These inversions inhibit vertical mixing and PBL growth with consequences for boundary layer O_3. Previously, Helmig et al. (2007) and Barten et al. (2021) have shown the important role of O_3 deposition to the snowpack on the composition of the lower troposphere. Van Dam et al. (2016) characterized an important role of atmospheric stability on summertime O_3 dynamics over the Arctic tundra. In contrast, the O_3 budget above the Arctic sea ice has not yet been characterized due to limited observational data (Jacobi et al., 2010). The ongoing retreat of the Arctic sea ice as a result of climate change (Keen and Blockley, 2018; Stroeve and Notz, 2018) urges us to improve our understanding of the exchange and further cycling of climate active trace gases, such as O_3, in the Arctic PBL in current and future climate. Considering that atmospheric chemistry and transport models are still strongly biased with respect to Arctic O_3 observations and showing large model-to-model variability (Whaley et al., 2022), improved process representation is necessary to better constrain Arctic tropospheric O_3 and its radiative effects.

In September 2019, the German research vessel (RV) *Polarstern* was docked within the Arctic sea ice for one year (October 2019–2020) as part of the Multidisciplinary drifting Observatory for the Study of Arctic Climate (MOSAiC) expedition. MOSAiC is centered around the goal to understand the causes and consequences of Arctic sea ice decline from an interdisciplinary perspective. This expedition provided, for the first time, detailed year-round observations of key meteorological and other drivers involved in O_3 dynamics in and above the PBL over sea ice (Shupe et al., 2022). For example, the campaign provided one year of surface O_3 concentration observations, enabling us to study the magnitude and variability of surface O_3 over the entire year. Supporting observations include turbulent O_3 flux observations to quantify the role of O_3 deposition to snow and ice, and O_3 sondes to analyze the vertical structure of O_3 in and above the PBL. The main objectives of this study were 1) to arrive at an improved quantification of Arctic snow/sea-ice O_3 deposition for various meteorological conditions and 2) to evaluate the contribution of dry deposition and other processes to the temporal variability of O_3 concentrations in the Arctic PBL during MOSAiC using a single-column atmospheric chemistry and meteorological model (SCM).

2. Methods

To reach the research objectives, we have combined MOSAiC observations with atmospheric modelling. We performed a year-round atmospheric simulation with a single-column atmospheric chemistry and meteorological model and attempted to represent most optimally MOSAiC observed meteorological and chemical conditions. This approach enabled us to use the model as a complementary tool to analyze the observations and to quantify processes that have not been or cannot be observed. We are confident that the behaviour of the SCM is representative for other 3D atmospheric chemistry and transport models, being applied to study Arctic O_3, in its representation and parameterizations of the meteorological and chemical processes. Applying the SCM, being constrained with reanalysis data, has allowed us to investigate in detail the contribution by all processes that explain the observed O_3 temporal variability.

2.1. Single column model

For analysis of in-situ observations, such as those collected during the 1-year MOSAiC field campaign, the SCM has demonstrated its merits in numerous studies (Ganzeveld et al., 2002; Ganzeveld et al., 2008; Kuhn et al., 2010; Seok et al., 2013; Barten et al., 2020). The SCM simulates the atmospheric physics and atmospheric chemistry processes in one column for a fixed location or, as in this case, following the track of the RV *Polarstern* in a quasi-Lagrangian mode. The SCM-simulated physics also drive atmospheric chemistry processes, including a selection of natural emissions, gas-phase chemistry, wet and dry deposition, and vertical turbulent and convective tracer transport in an online mode. The result is a feedback between the simulated meteorology and atmospheric chemistry and vice versa. Stratospheric and tropospheric chemistry are represented in this study by the MECCA1 box modelling system (Sander et al., 2005), including an O_3-NO_x-halogen chemistry scheme considering 74 tracers. In addition, the SCM has been coupled to the Coupled Ocean-Atmosphere Response Experiment Gas transfer algorithm (COAREG) (Fairall et al., 2011) for a more explicit representation of ocean-atmosphere fluxes of O_3, as well as carbon dioxide (CO_2), methane (CH_4), and dimethyl sulfide (DMS), all being climate-active trace gases, the fluxes of which were measured during MOSAiC. These fluxes are quantified in the model considering atmospheric- and waterside turbulence and the atmosphere-ocean concentration gradient. Furthermore, the SCM contains a straightforward 2-layer representation of snowpack-atmosphere exchange considering the role of diffusion, wind pumping, sorption, emissions, and gas- and aqueous-phase chemistry on snow-atmosphere exchange of trace gases. This 2-layer representation formed the basis of the development of a more detailed snowpack trace gas exchange model by Murray et al. (2015) that was applied in a study of O_3 and NO_x snow-atmosphere exchange at Summit, Greenland. The simplified 2-layer version applied here mainly makes strong assumptions on the physicochemical representation of the snow layer compared to the extended version by Murray et al. (2015). In this study, we have applied the simplified 2-layer version mainly to study whether this explicit representation of in-snowpack O_3 concentrations might explain short-term events of bidirectional exchange of O_3. We selected an overall snow uptake rate of 0.005 cm s^{-1} such that the snowpack model reproduced the observation inferred from long-term snowpack uptake resistance (Murray et al., 2015).

Here, the SCM was set up with 60 atmospheric layers having 11 layers in the lowest kilometer, of which 5 layers are in the lowest 100 meters. This layering allows for a relatively detailed resolution in the PBL and lower free troposphere, which is the focus of this study. The model simulation was initialized with European Centre for Medium-Range Weather Forecasts Reanalysis (ERA5) meteorological (Hersbach et al., 2020) and Copernicus Atmosphere Monitoring Service (CAMS) chemical composition (Inness et al., 2019) reanalysis data and run for the period of October 1, 2019, 00:00 UTC to October 1, 2020, 00:00 UTC at time steps of 60 seconds. We studied model results at a temporal resolution of 1 hour. The SCM also explicitly estimates heat transport through 5 σ-coordinate sea-ice layers with one snow layer on top. The ice-covered fraction of the SCM was initialized with a sea-ice thickness of 1.0 m and a 20-cm-thick snow layer on top based on a preliminary analysis of ice mass balance buoys deployed at the start of MOSAiC (Lei et al., 2021; Nicolaus et al., 2022). Furthermore, the SCM updates the geostrophic and vertical wind speeds, sea-ice fraction, sea surface temperature, and surface pressure from ERA5 throughout the simulation.

We nudged the SCM to the ERA5 and CAMS reanalysis data to consider the role of advection and changes in synoptic conditions. More specifically, we nudged the model to air temperature, *u* and *v* winds and liquid water content above the PBL. We did not nudge the SCM to ERA5 for heights below 250 m to avoid a stronger forcing of surface layer variables for very shallow PBLs. Furthermore, we nudged the SCM to mixing ratios of O_3, NO_x, carbon monoxide (CO) and formaldehyde (HCHO) in and above the PBL to assure that these model simulations optimally consider the role of changes in synoptic conditions and advection regimes in determining local meteorological and chemical conditions. We applied relaxation coefficients of 1 h and 3 h for physical parameters and chemical tracers, respectively. The relaxation coefficient to physical parameters is 6 times larger compared to Sterk et al. (2015), who applied a 1D version of the Weather Research and Forecasting model to simulate clear-sky stable PBLs over snow covering a 2-day period. We have tested a range of relaxation coefficients, and with the relaxation coefficients of 1 h and 3 h, aiming to ensure that the SCM follows the seasonal cycle in meteorology and atmospheric chemistry from the ERA5 and CAMS reanalysis products, but not to nudge too strongly to avoid that these simulations would mainly reflect the quality of the ERA5 and CAMS products. A preliminary analysis showed that additional nudging to specific humidity (*q*) leads to unrealistically abundant cloud formation in the SCM creating numerical issues associated with differences in the representation of the surface energy balance in the SCM and ERA5 (Ganzeveld et al., 2006). Therefore, no nudging to *q* has been applied in the SCM simulation to secure a more realistic representation of cloud cover and surface radiation. ERA5 assimilates the radiosondes launched during MOSAiC and the RV *Polarstern* automatic weather station data. Here, we used the same radiosondes to determine the PBL height during MOSAiC that were also used to nudge the SCM above the PBL. However, the SCM still explicitly calculates boundary layer mixing and the PBL height. In Figure S1, we show a direct comparison of SCM-simulated, MOSAiC-observed, and ERA5 reanalysis 2-m air temperature, 10-m wind speed, and 10-m wind direction. CAMS assimilates observations from several satellites but it does not assimilate O_3 observations from MOSAiC, other in situ measurement sites, or ozone sondes (Inness et al., 2020). In Figure S2, we show a direct comparison of SCM-simulated, MOSAiC-observed, and CAMS reanalysis surface O_3 mixing ratios.

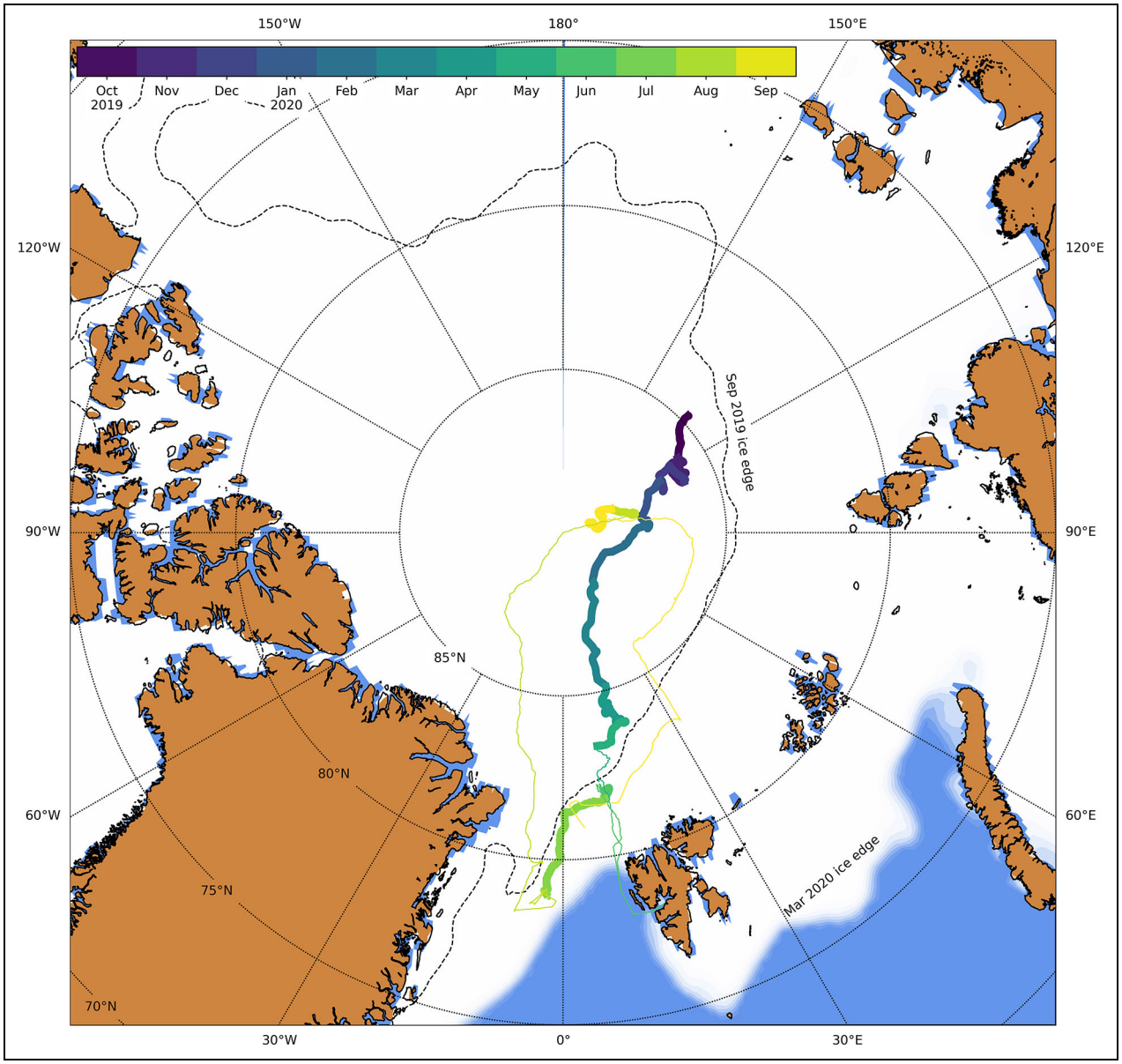

Figure 1. Drift trajectory of MOSAiC. Drift trajectory of MOSAiC from October 15, 2019, to September 30, 2020, colored per month. The thick lines indicate the drift trajectory and the thin lines show the path of the RV *Polarstern* when in transit. The white contours in the background indicate the March 2020 sea-ice maximum from ERA5 and the dashed black line indicates the September 2019 sea-ice edge minimum from ERA5 (sea-ice fraction = 0.3).

2.2. Observations

2.2.1. Meteorological data

To evaluate the SCM-simulated micro-meteorology, we used observations taken at a meteorological tower operated on the sea ice 300 m to 500 m from RV *Polarstern* as part of the MOSAiC Central Observatory (Shupe et al., 2022). Here, we used 1-min observed 2-m air temperature (T_{2m}), 10-m wind speed (V_{10m}), and 10-m wind direction (Cox et al., 2021) re-sampled to hourly mean observations. Data gaps occurred during periods when the RV *Polarstern* was in transit, i.e., May 10 to June 24 (2020) for the Leg 3 to Leg 4 exchange at Svalbard and July 29 to August 25 (2020), when the original ice floe broke apart and a new Central Observatory was set up around 88 N (Shupe et al., 2022). See **Figure 1** for an overview of the MOSAiC drift trajectory.

2.2.2. Surface O_3 concentrations and fluxes

Ambient air for the O_3 flux analyzers was drawn from a Teflon inlet at the top of the RV *Polarstern* bow tower. The tower was installed at the end of a horizontal crane extending approximately 5 m in front of the ship's bow (see Shupe et al., 2022). Inlets were co-located on the tower with a 3D ultrasonic anemometer, approximately 20 m above the ice surface. A heated Teflon inlet line (approximately 1-cm inner diameter, 45-m long) carried sample air to the O_3 flux analyzer located in a below-deck laboratory space at a mean flow of 30 standard liters-per-minute (SLPM). This flow was sub-sampled into the O_3 flux analyzer at a flow of 1.2 SLPM through a Nafion air dryer. See Bariteau et al. (2010) and Boylan et al. (2014) for a detailed description of the fast O_3 flux analyzer.

Synchronization of fast O_3 response with fast wind speed and correction for low-pass filtering effects of the inlet tubing were facilitated by subjecting the sampling system once every hour to a 5-s pulse of pure nitrogen at the inlet tip. See Bariteau et al. (2010) and Blomquist et al. (2010; 2014). The O_3 flux was estimated as the covariance of synchronized dry-air O_3 mole fraction and vertical wind velocity. The flux detection limit was evaluated hourly as the covariance of time-shifted (decorrelated) O_3 mole fraction and vertical velocity. Additional filtering with respect to wind speed (>1 m s^{-1}) and wind direction ($\pm 90°$) was applied to limit interference from RV *Polarstern* on the eddy-covariance system. Furthermore, non-stationary conditions were filtered out. Finally, we have filtered out the O_3 flux data for boundary layers shallower than 40 m—twice the reference height of the flux observations—based on the SCM-simulated PBL heights. The motivation for this additional filtering was to exclude those O_3 flux observations not deemed being representative for the actual O_3 surface fluxes, but more reflecting the role of entrainment due to presence of a very shallow inversion layer. This filtering resulted overall in removing approximately 12% of the O_3 flux observations. The radiosonde-inferred PBL height was not applied for this filtering due to its high uncertainty in the case of very shallow boundary layers and the limited temporal coverage.

Redundant measurements of ambient air O_3 concentrations were performed in three distinct sea-laboratory containers (Angot et al., 2022a; Beck et al., 2022). Here we used an hourly-averaged merged dataset that combines the cross-evaluated individual O_3 datasets. A detailed description of the set-up and filtering of O_3 flux data, as well as measurements of the CO_2, CH_4 and DMS fluxes, is planned for an upcoming manuscript.

2.2.3. Observation-derived ozone deposition resistance terms

In state-of-the-art atmospheric chemistry transport models, the deposition process is generally considered by calculation of a deposition velocity following the resistance in series approach first proposed by Wesely (1989). The O_3 deposition velocity $V_{d,O3}$ (m s^{-1}) is estimated as

$$V_{d,O3} = \frac{1}{r_a + r_b + r_c}, \tag{1}$$

where r_a is the aerodynamic resistance (s m^{-1}), r_b is the quasi-laminar sub-layer resistance (s m^{-1}), and r_c is the surface resistance (s m^{-1}). Both r_a and r_b, representing turbulent transport and diffusion close to the surface, strongly depend on meteorological conditions. The term r_c represents the efficiency of removal by the surface and is typically two to three orders of magnitude larger than r_a and r_b for simulated O_3 deposition to snow and ice (Helmig et al., 2007; Hardacre et al., 2015). The simulated O_3 flux $\overline{w'O_3'}$ (ppb m s^{-1}) at the surface is calculated as

$$\overline{w'O_3'} = V_{d,O3} \cdot [O_3]_{surf}, \tag{2}$$

where $[O_3]_{surf}$ is the O_3 mixing ratio at the surface (ppb). Here, we used the observed O_3 deposition fluxes to derive an estimate of r_c as the residual term in explaining the observed flux. Similar to de Jalón et al. (2019), we estimated r_a and r_b from observed meteorological properties according to:

$$r_{a,obs} = \frac{V_z}{u^{*2}} \tag{3}$$

and

$$r_{b,obs} = \frac{2}{k \cdot u^*} \cdot \frac{Sc^{2/3}}{Pr}, \tag{4}$$

where V_z is the wind speed at height z (m s^{-1}), u^* is the friction velocity (m s^{-1}) from the eddy-covariance system, k is the von Karman constant of 0.4, and $Sc = 1.07$ and $Pr = 0.72$ are the Schmidt number of O_3 and Prandtl number in air, respectively (Hicks et al., 1987). Then, we derived r_c from Equations 1 and 2 using the observed surface O_3 mixing ratio and flux as

$$r_{c,obs} = \frac{[O_3]_{surf}}{\overline{w'O_3'}_{obs}} - r_{a,obs} - r_{b,obs}. \tag{5}$$

A stability correction of r_a is suggested to be significant for very stable conditions under bulk Richardson numbers >0.2 (Toyota et al., 2016) in atmospheric chemistry models. By using the observed wind speed and friction velocity, we accounted for the stability effects in the observation-derived method. Furthermore, this stability correction of r_a is accounted for in the representation of the deposition process in the SCM (Ganzeveld and Lelieveld, 1995).

2.2.4. Radiosondes

We used data from radiosondes launched during MOSAiC (Maturilli et al., 2021) to infer the magnitude and temporal evolution of the PBL Height (PBLH). Radiosondes were launched four times per day (6-hourly) and provide detailed information on the vertical structure of atmospheric temperature, humidity, and horizontal wind speed. We applied the bulk-Richardson-number method, which is a common method to derive the PBLH from radiosondes (e.g., Zilitinkevich and Baklanov, 2002; Zhang et al., 2014). Furthermore, Jozef et al. (2022) found this automated objective method to be most accurate compared to subjective identification of the PBLH during MOSAiC. The bulk Richardson number Ri_B (−) from the surface up to height h (m) is defined as the ratio between the estimated buoyancy and shear production as given in Equation 6:

$$Ri_B = \frac{(g/T_{v,0}) \cdot (\theta_v(h) - \theta_v(0)) \cdot h}{u(h)^2 + v(h)^2}. \tag{6}$$

Here, g is the gravitational acceleration (m s^{-2}), $T_{v,0}$ is the virtual temperature at the surface (K), $\theta_v(h)$ and $\theta_v(0)$ are the virtual potential temperature (K) at height h and at the surface, respectively, and $u(h)$ and $v(h)$ are u and v wind components (m s^{-1}) at height h. The bulk-Richardson-number method assumes that the PBLH is the height at which the bulk Richardson number reaches the critical bulk Richardson number Ri_{Bc}. When $Ri_B > Ri_{Bc}$, turbulence production by shear is insufficient to

compensate for the suppression of turbulence by buoyancy. For this study, we applied a Ri_{Bc} of 0.40 based on a preliminary analysis of a subset of the observed profiles and manual identification of the PBLH based on temperature and humidity gradients at the PBL top. We note that even though a constant Ri_{Bc} is often applied it rather depends on atmospheric stability (Richardson et al., 2013; Basu et al., 2014), with values for Ri_{Bc} typically ranging from 0.1 to 1.0 (Zilitinkevich and Baklanov, 2002). However, a detailed analysis of appropriate Ri_{Bc} for best estimates of PBLH during MOSAiC, e.g., compared with other PBLH estimates from sodar (Brooks et al., 2017), is out of scope for this study. Additional uncertainty arises from the fast ascent of the radiosonde and uncertainty in the GPS-retrieved altitude, especially close to the surface. Therefore, the exact magnitude of the radiosonde-derived PBLH might be subject to a substantial uncertainty. However, we do not focus on the magnitude but rather on the temporal evolution of the PBLH and identification of periods with suppressed mixing relevant for the analysis of surface O_3 concentration and flux observations.

To complement the surface O_3 concentration and flux observations, we used additional observations on the vertical distribution of O_3 using sondes launched during MOSAiC (von der Gathen and Maturilli, 2020; 2022). Approximately one radiosonde per week was equipped with an O_3 sensor, with some periods (e.g., springtime) having a higher temporal coverage. In total, 56 O_3 sondes were launched between October 1, 2019, and September 30, 2020. For better comparison with the SCM, we have regridded the data from the O_3 sondes to 30-m vertical bins to allow for identification of O_3 gradients above the PBL. In this study, we focused on the vertical profiles of O_3 in the PBL and free troposphere and discarded observations of stratospheric O_3, which have been shown to be highly depleted in the 2020 spring season due to severe chemical loss in a strong and long-lasting polar vortex (Inness et al., 2020; Wohltmann et al., 2020).

3. Results

First, we present the model evaluation of meteorological diagnostics essential for the analysis of the PBL budget of O_3. Second, we compare the simulated and observed O_3 deposition resistance terms as one of the main components of the O_3 budget. Thereafter, we compare the modelled and observed surface O_3 concentrations and quantify the contribution of each process to the O_3 budget in the PBL. Finally, we evaluate the link between surface observations and free tropospheric O_3 by a comparison of SCM simulations and observations on the vertical O_3 distribution.

3.1. Evaluation of SCM-simulated meteorology

The SCM shows a good performance with respect to observed T_{2m} (**Figure 2a** and **e**) with an explained variance R^2 of 0.88. The SCM and observations agree on the seasonal cycle, with a minimum T_{2m} of about $-40°C$ reached at the end of winter and a persistent period of T_{2m} around 0°C in summer due to the melting sea ice (Shupe et al., 2022). Even though the SCM is able to represent most of the temporal variability in observed T_{2m}, the observations show larger variability on hourly timescales, arguably due to the misrepresentation of local processes in the SCM or a misrepresentation of surface properties such as albedo, sea-ice cover and sea-ice thickness affecting the surface energy balance. The SCM generally simulates warmer conditions than observed with a bias of $+1.0°C$. Most notably, the warm bias increases

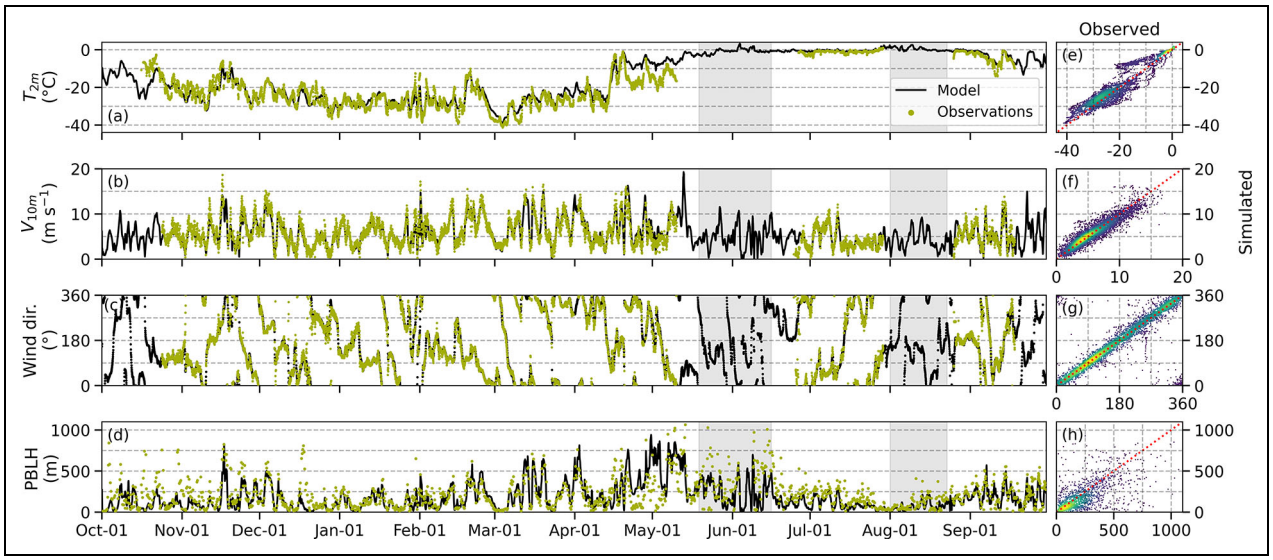

Figure 2. Comparison of simulated and observed meteorology. Temporal evolution of simulated (black) and observed (olive green) (a) 2-m air temperature (°C), (b) 10-m wind speed (m s^{-1}), (c) 10-m wind direction (°) and (d) planetary boundary layer height (m) and (e–h) corresponding 1:1 scatter plots of observed (x-axis) and simulated (y-axis) variables shown in (a–d). The grey shadings in (a–d) indicate the periods when RV *Polarstern* was in transit. The colors in (e–h) express the kernel density estimation, where brighter colors correspond to a higher point density with (e) $R^2 = 0.88$, (f) $R^2 = 0.84$, (g) $R^2 = 0.85$, (h) $R^2 = 0.35$, and the red line indicates the 1:1 line.

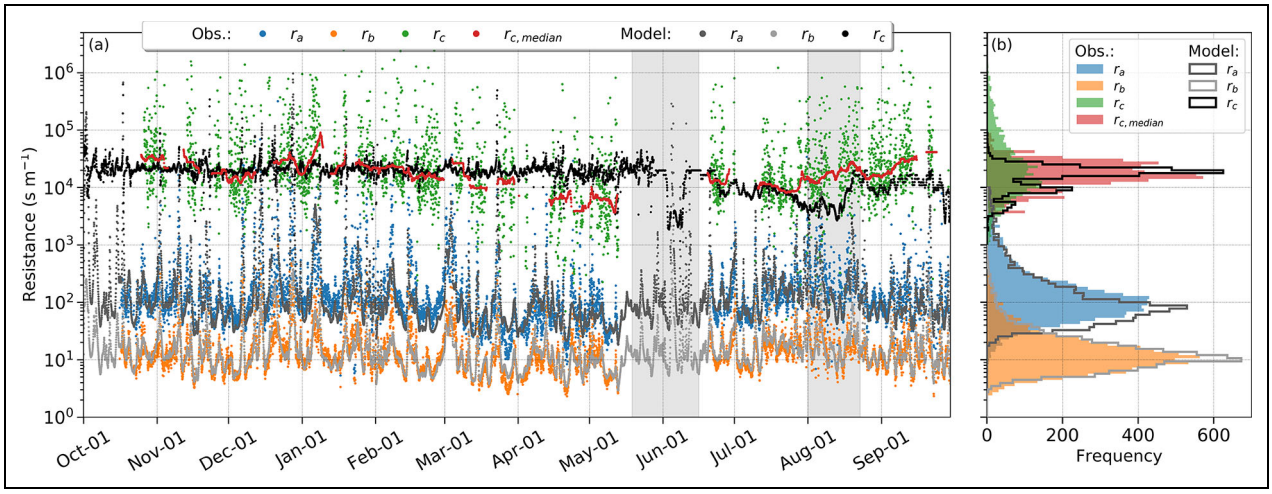

Figure 3. Comparison of simulated and observed ozone deposition resistance terms. (a) Temporal evolution and (b) co-sampled frequency distribution of observation-derived (colors) and simulated (grey scales) aerodynamic resistance (r_a (s m^{-1}); blue, grey), quasi-laminar sub-layer resistance (r_b (s m^{-1}); orange, light grey), surface resistance (r_c (s m^{-1}); green, black) and 7-day running median observed surface resistance ($r_{c,median}$ (s m^{-1}); red). The grey shadings indicate the periods when RV *Polarstern* was in transit.

to +2.1°C for observed $T_{2m} < -25$°C, indicating a potential overestimation of turbulent mixing during very stable conditions (Kral et al., 2021). Note that the SCM-simulated meteorology is strongly affected by nudging the SCM to the ERA5 reanalysis data above the boundary layer. For a direct comparison of SCM-simulated, MOSAiC-observed and ERA5 reanalysis meteorology see Figure S1.

The SCM also shows a relatively good performance with respect to observed V_{10m} (**Figure 2b** and **f**) with an R^2 of 0.84. The SCM is able to represent the observed maxima and minima in V_{10m}, showing no significant positive or negative bias. Periods with a large positive T_{2m} bias up to +10°C (e.g., around May 1) appear to coincide with a positive V_{10m} bias of 1 to 2 m s^{-1}, related to an underestimation of surface stratification. However, the bias in V_{10m} cannot completely explain the warm bias in T_{2m}, indicating the role of other processes such as energy exchange at the surface or thermal radiation divergence. Similarly to V_{10m}, the wind direction is well represented by the SCM (**Figure 2c** and **g**) with an R^2 of 0.85. This result indicates that we anticipate a good model representation of the contribution by advection of O_3 and other long-lived precursors with air masses coming from different origins.

Simulated and observed PBLH show large variations, with boundary layer depths ranging from approximately 10 m to 1000 m (**Figure 2d** and **h**). The 25th and 75th percentiles for the observations and SCM amount to [86, 305] and [57, 241] m, respectively. These values indicates that for this study the Arctic boundary layer was typically shallower than a few hundred meters and boundary layers of a few tens of meters were common. Both the SCM and observations show the largest variation and deepest boundary layers in spring/early summer (March to June). Also during calm conditions with $V_{10m} < 5$ m s^{-1} (e.g., around March 1 and August 1) both the SCM and observations agree well on the presence of boundary layers often shallower than 50 m. In general, the temporal evolution and variability in radiosonde-derived PBLH was captured by the SCM even though biases were more pronounced during certain periods (e.g., May to June). Moreover, a substantial positive bias in PBLH was found around May 1 when the SCM significantly overestimated T_{2m} and V_{10m}. This finding again indicates the presence of excessive turbulent mixing in the SCM during that period.

3.2. Ozone deposition resistance terms

The observations show that the aerodynamic resistance (r_a) is typically on the order of 10^2 s m^{-1}, with extremes exceeding 10^3 s m^{-1} during periods with very low wind speeds (**Figure 3a**). For the quasi-laminar sub-layer resistance (r_b), being typically one order of magnitude smaller than r_a, we find a typical magnitude of 10^1 s m^{-1} and peaks exceeding 10^2 s m^{-1}. We find that the SCM simulates generally well the observed magnitude and temporal variability in r_a and r_b both in the timing of the maxima and minima. The co-sampled frequency distributions (**Figure 3b**) show that the SCM slightly underestimates the observed peak in r_a of 10^2 s m^{-1}. Rather, the SCM shows a peak around 80 s m^{-1}. We argue that this discrepancy is related to overestimated surface mixing conditions in the SCM leading to an underestimation in r_a. The SCM resembles rather well the observed frequency distribution of r_b, both peaking at 10^1 s m^{-1} and only exceeding high values of r_b of 10^2 s m^{-1} approximately 4% of the time.

We find a large variability in observed surface resistance (r_c), with minima as small as 10^3 s m^{-1} and maxima up to 10^6 s m^{-1}. The frequency distribution (**Figure 3b**) peaks between 10^4 s m^{-1} and 2×10^4 s m^{-1}. By computing a 7-day running median, we find a r_c of approximately 2×10^4 s m^{-1} ($V_{d,O3} \asymp 0.005$ cm s^{-1}) in winter before dropping below 10^4 s m^{-1} for the months of April and May. This snow-sea ice uptake resistance inferred from these long-term O_3 flux observations is much larger compared to the still commonly applied snow-ice uptake rate

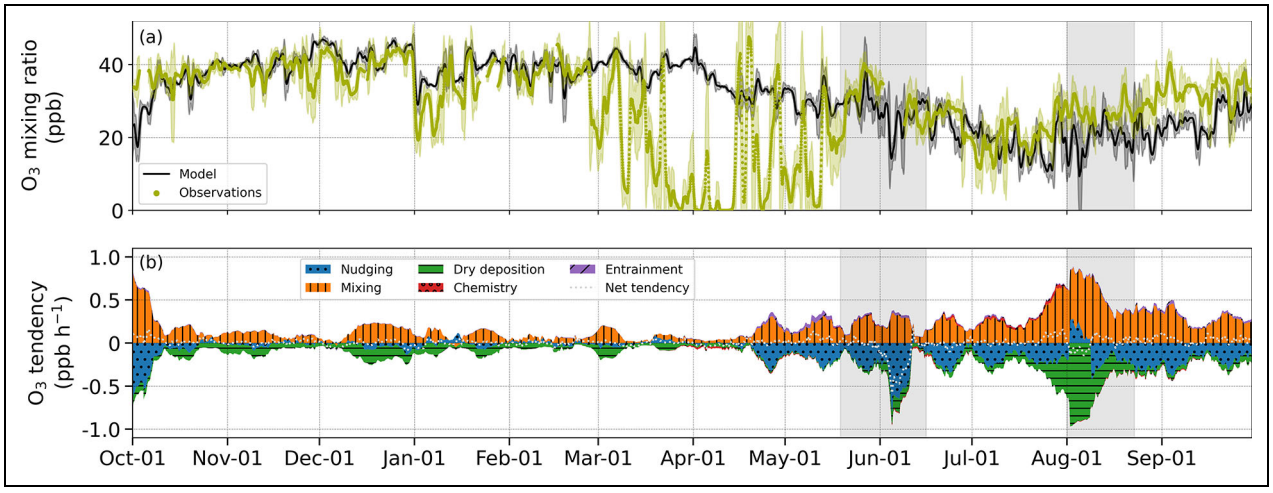

Figure 4. Surface ozone and the ozone budget. Temporal evolution of (a) simulated (black) and observed (olive green) daily running mean surface O_3 mixing ratios (ppb) ± two standard deviations (shadings) and (b) 7-day running means for simulated net (dotted line), nudging (blue, implicitly representing advection), turbulent (orange), dry deposition (green), chemistry (red) and entrainment (purple) O_3 tendencies (ppb h^{-1}) in the planetary boundary layer. The grey shadings indicate the periods when RV *Polarstern* was in transit.

of 2×10^3 s m^{-1}, resulting in a dry deposition velocity of 0.05 cm s^{-1} in most atmospheric chemistry and transport models (Simpson et al., 2012; Hardacre et al., 2015; Falk and Søvde Haslerud, 2019). The observation-inferred uptake resistance of 2×10^4 s m^{-1} is more in line with estimations of 1×10^4 s m^{-1} by Helmig et al. (2007) implemented in more recent model experiments (Barten et al., 2021; Herrmann et al., 2021; Marelle et al., 2021). The reduction in observation-derived r_c in spring and summer might potentially be related to a larger open water flux footprint and the reactions between O_3 and ocean water reactants (Loades et al., 2020). At the end of summer, the observed r_c is again on the order of 2×10^4 s m^{-1}. The increase in the summer appears to be insignificant due to the large variability in the observations. The SCM results show less variation compared to observed r_c. This result indicates that the simulated temporal variability in processes considered in the first-order 2-layer snowpack-atmosphere exchange model, e.g., the role of wind pumping, does not explain the observed temporal variability in r_c. However, the model agrees on a rather constant r_c of 2×10^4 s m^{-1} ($V_{d,O3} \asymp 0.005$ cm s^{-1}) in the weekly median from November to April. During August, the SCM-simulated r_c is biased low for a period with significant open water fraction (>0.5 for 2 weeks) in the ERA5 forcing dataset. This bias highlights the sensitivity in the SCM to O_3 deposition to water surfaces that might not be representative for the 7-day median observations with a more local footprint. The r_a and r_b terms, being typically 2 and 3 orders of magnitude smaller than r_c, appear to put no significant constraint on the total resistance term over the entire year. This lack of constraint indicates that the removal rate is dominated by the actual snow/sea-ice uptake efficiency with an insignificant role of turbulent transport to and molecular diffusion near the surface. Therefore, the impact of a misrepresentation of SCM-simulated atmospheric stability on the O_3 deposition flux is limited.

3.3. Surface ozone concentrations and tendencies

The observed evolution in daily mean surface O_3 mixing ratios shows a seasonal cycle with a maximum in winter, followed by ODEs in spring and another minimum at the end of summer (**Figure 4a**). Daily mean O_3 mixing ratios reach 45 ppb in wintertime and 15 to 20 ppb at the end-of-summer minimum. In March, April and May, the observations show clear indications of ODEs with observed O_3 mixing ratios as low as <1 ppb. These ODEs occur on timescales of several hours to days in shallow boundary layers (**Figure 2d**) during episodes with low wind speeds (**Figure 2b**). The recovery of ozone to mixing ratios up to 45 ppb occurs at a similar timescale. The SCM results agree with the seasonal cycle in observed surface O_3 mixing ratios in terms of the winter maximum and end-of-summer minimum. However, the SCM is unable to represent the ODEs in spring due to the fact that we have not considered the halogen emissions in these model experiments. Moreover, the role of halogen chemistry is not considered in the CAMS reanalysis data used for nudging (Figure S2). The SCM and observations also agree on sharp changes in surface O_3 mixing ratios in winter (e.g., around January 1) caused by advection of different air masses in CAMS depicted by a sudden shift in wind direction (**Figure 2c**) and a changing footprint area of the surface O_3 concentration observations. Interestingly, the SCM shows less variability in the daily mean surface O_3 mixing ratios compared to observations, due to a misrepresentation of local processes affecting the surface O_3 concentrations. This reduced variability can be caused by a lower variability in O_3 deposition (**Figure 3**) in the SCM, a misrepresentation of local processes such as snow ridging causing additional surface roughness, or local chemistry

caused by halogen emissions from the snowpack which are not included in the SCM. Especially in wintertime, the temporal variability in surface O_3 simulated by the SCM is very low. In wintertime, the model shows no significant positive or negative bias. In springtime, the model is strongly positively biased due to the missing halogen sources and resulting ODEs. From June onwards, the SCM modelled O_3 is slightly negatively biased by 3 to 4 ppb.

The observed and simulated O_3 mixing ratios (**Figure 4a**) are governed by many processes. Ultimately, we want to determine the role of these different processes on the PBL-integrated mixing ratios over the entire year for various meteorological conditions. Therefore, we have estimated the PBL O_3 integrated process tendencies in the SCM. Basically, we have estimated for every time step the contribution by nudging, vertical mixing, dry deposition, chemistry (the net result of all chemical reactions), and entrainment from the free troposphere to the simulated changes in O_3 mixing ratios, as described in Equation 7:

$$\frac{d[O_3]}{dt} = Nudging + Mixing + Deposition + Chemistry + Entrainment. \quad (7)$$

To interpret how temporal changes in observed O_3 mixing ratios are explained by the different processes controlling boundary layer O_3, the process tendencies are given in ppb h^{-1}. These values were calculated by integrating the O_3 and air mass over the PBLH accounting for the decreasing density and increasing thickness of layers with altitude. Here, the nudging tendency mainly reflects the contribution by advection if differences between the SCM- and CAMS-simulated processes in the vertical column are small relative to this contribution by advection. Although vertical mixing and entrainment are calculated as different tendencies, both represent mixing of O_3-rich air from layers aloft to layers in the PBL. The turbulent transport tendency, calculated from the divergence of the fluxes at the interfaces of the SCM model layers representing the boundary layer, mostly reflects the compensating effect by downward transport throughout the boundary layer to the surface to compensate for dry deposition. In contrast, the entrainment tendency solely represents the increase in O_3 concentration due to the increase of the PBLH over time and thus entrainment of free tropospheric air masses enhanced in O_3 using a bulk approach. Because the SCM is unable to capture the high temporal variability in deposition (**Figure 3**) and surface mixing ratios (**Figure 4a**) on hourly timescales, we have applied a 7-day running mean to these tendencies to determine the dominant processes on timescales of days to weeks (**Figure 4b**).

Over the entire year, vertical mixing, representing the redistribution of O_3 towards the surface, always contributes positively to the net O_3 PBL budget. The nudging tendency can be either a positive or a negative contribution. The net effect of chemistry (both positive and negative) and entrainment (only positive) only contribute marginally (<5%) to the simulated 7-day running mean net tendency. In winter, vertical mixing and dry deposition appear to be the processes that dominate the magnitude and temporal variability of PBL O_3 as reflected by their contribution to the net tendency. The removal at the surface by dry deposition is mainly counteracted by the redistribution of O_3 by downward turbulent transport. We expect a larger contribution by chemistry in spring given the ODEs (**Figure 4a**); however, not having considered the potential sources and resulting chemical destruction of O_3, the tendencies for ODEs do not represent the anticipated on-site observed conditions. While in wintertime dry deposition appears to mainly determine the O_3 sink, compensated for by vertical mixing, nudging also plays a substantial role in the period of June to September. Interestingly, we find a strong negative contribution by dry deposition up to -1.0 ppb h^{-1} in August. Here, both observations and the SCM are characterized by a period of persistent low wind speeds (**Figure 2b**) and shallow boundary layers (**Figure 2d**). Also in wintertime, we find that during periods with relatively shallow boundary layers the role of dry deposition on the O_3 concentrations increases. On the other hand, this finding also implies stronger O_3 gradients from the surface layer to layers aloft, which will ultimately be compensated by turbulent mixing.

3.4. Vertical distribution of tropospheric ozone

Although we have shown that the SCM is overall very well able to represent the observed seasonal cycle in surface O_3 during MOSAiC, the SCM clearly fails in representing observed springtime surface O_3 concentrations related to ODEs. To further study the dynamics of O_3 in the PBL and in the free troposphere, including its representation in the SCM, we used data from O_3 sondes launched during MOSAiC (**Figure 5**). In wintertime, we find modelled and observed free tropospheric O_3 mixing ratios up to 50 ppb with weak gradients towards the surface. On average, we find a $\Delta O_{3(1500m-surf)}$ of 5.2 and 8.4 ppb in wintertime for the SCM co-sampled with observations and O_3 sondes, respectively. O_3 sonde observations close to the surface have a high uncertainty due to the fast ascent, measurement delay and chaotic rotation of the sonde after launch (Carminati et al., 2019). In springtime, the observations show strong O_3 gradients above the PBL. The vertical extent of the ODEs appears to be confined to the first few hundreds of meters above the estimated PBLH. The observed O_3 mixing ratios above 1000 m are hardly affected by the ODEs in spring, which also indicates a role of entrainment in the recovery of surface O_3 after ODEs. Unfortunately, this entrainment cannot be quantified using the SCM because the ODEs are not represented in these model experiments. Additionally, the temporal coverage of the O_3 sondes is too coarse to allow a quantification of the role of entrainment during ODEs. During springtime, we find a mean $\Delta O_{3(1500m-surf)}$ of 31.2 ppb from the O_3 sondes. Similarly to **Figure 4a**, we find that summertime O_3 is more depleted compared to wintertime, also in the free troposphere (**Figure 5**). During summertime, we find that both model and observations show stronger gradients towards the surface compared to wintertime, with a mean $\Delta O_{3(1500m-surf)}$ of 16.3 and 11.6 ppb in the SCM and O_3 sondes, respectively. However, in

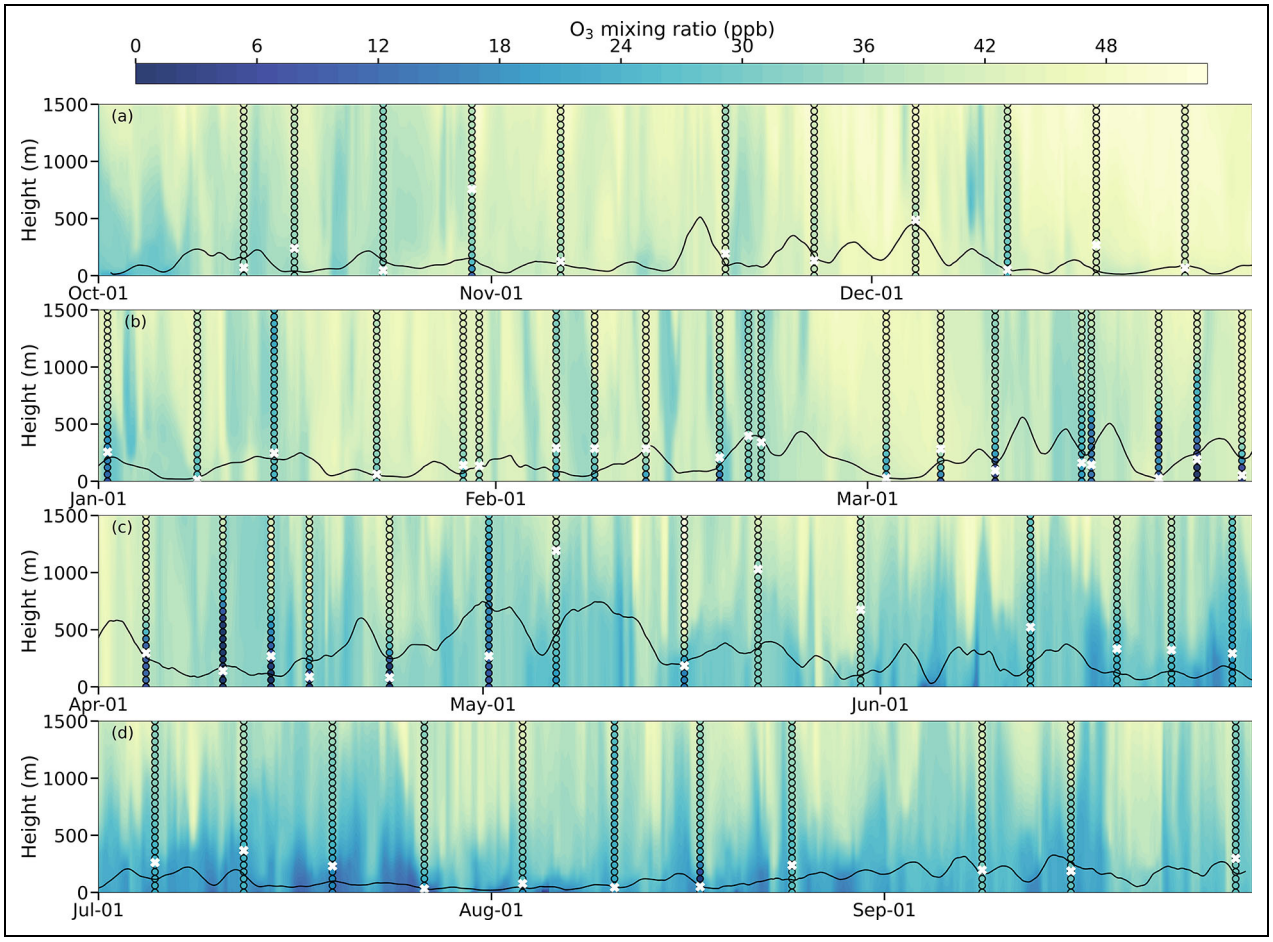

Figure 5. Vertical distribution of ozone. Time-height cross section of simulated (background) and observed (filled circles) O_3 mixing ratios (ppb) for (a) October–November–December 2019, (b) January–February–March 2020, (c) April–May–June 2020 and (d) July–August–September 2020. The black line and white crosses represent the simulated and observation-derived planetary boundary layer heights, respectively.

summer the SCM produces a negative bias in surface O_3 of 3 to 4 ppb (**Figure 4a**) which explains the stronger gradient in the SCM.

Figure 6 confirms that the SCM is most prominently biased in the lowest few hundreds of meters. Including all O_3 sondes results in a positive bias over 10 ppb close to the surface, while excluding the O_3 sondes in springtime still results in a bias of 6 ppb (not shown here). The bias in the free troposphere reduces with increasing altitude and reaches a minimum around 3 km. Above this height, the absolute bias towards the tropopause increases due to elevated O_3 mixing ratios. Most notably, we find a positive bias over the entire troposphere for the October 2019 to February 2020 months with low variability. The bias in May 2020 to September 2020 is smaller, but shows more variability. Again, the fast ascent of the O_3 sonde leads to a high uncertainty in the O_3 observations close to the surface because we do not find a bias of 6 ppb in the surface O_3 observations (**Figure 4a**). This significant bias in the PBL can hint towards an underestimation of the dry deposition sink term, even though we have shown that simulated dry deposition corresponds well with the long-term (weekly mean) observed dry deposition rates (**Figure 3a**). Another reason could be the underestimation of sources of halogens, resulting in removal of O_3 in the PBL. Furthermore, enhanced turbulent mixing in the SCM (also reflected by overestimated T_{2m}; **Figure 2a**) might result in an overestimation of entrainment from O_3-rich air from the free troposphere into the PBL.

4. Discussion

This study demonstrates the role of O_3 dry deposition to snow and ice on the year-round O_3 budget in the Arctic PBL using observations as part of the MOSAiC campaign and supported by application of a single-column atmospheric chemistry and meteorological model. By constraining the SCM with the ERA5 meteorological (Hersbach et al., 2020) and CAMS chemical (Inness et al., 2019) reanalysis data, we aim to arrive at the most accurate representation of on-site conditions observed during MOSAiC based on correct process representation. The SCM simulates all of the atmospheric column physical and chemical processes as a function of the explicitly resolved sea-ice/snow and ocean surface source and sink processes. However, application of these reanalysis data to constrain the SCM-simulated processes implies that the simulated meteorology and chemistry also reflects the accuracy of these reanalysis datasets to represent the in-situ

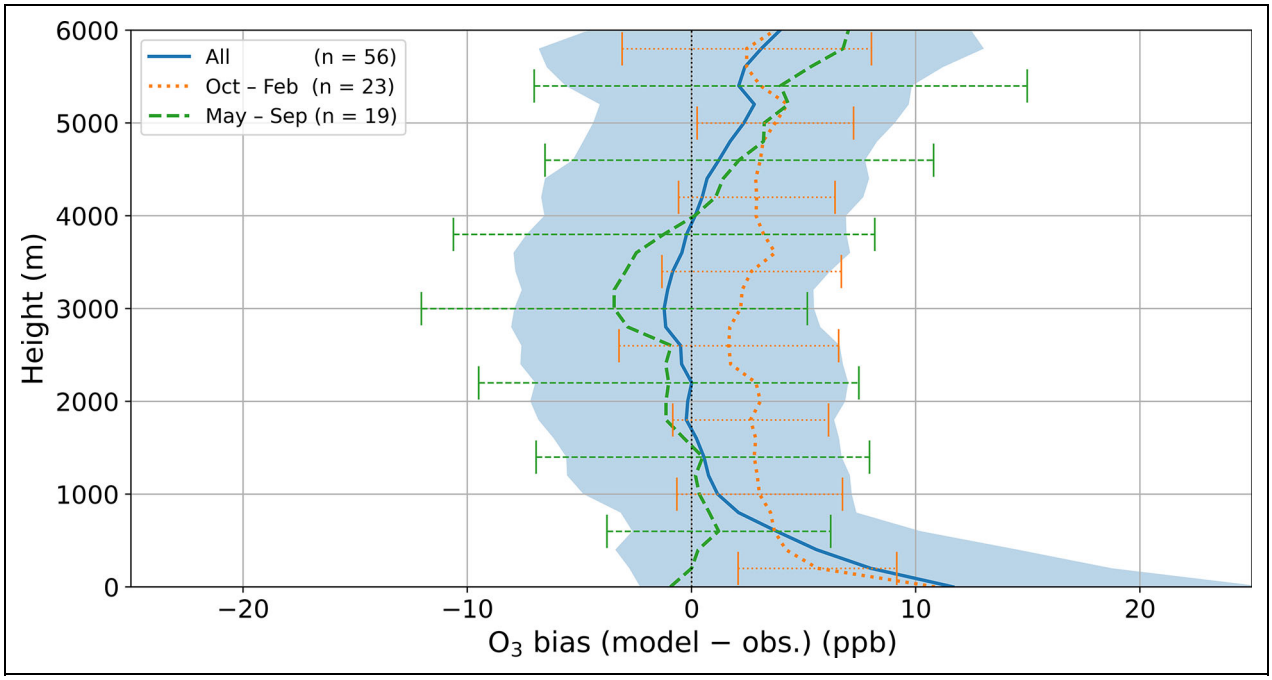

Figure 6. Vertical distribution of simulated ozone bias. Vertical distribution of mean O_3 bias (simulated minus observations) (ppb) for all ozone sondes (blue), October 2019 to February 2020 (orange) and May 2020 to September 2020 (green). The shadings and error bars indicate ± one standard deviation. Note the extended y-scale with respect to **Figure 5**.

meteorological and atmospheric composition observations. Furthermore, the results reflect the average conditions for a domain of 0.25° × 0.25° (ERA5) or 0.75° × 0.75° (CAMS). This resolution suggests that the SCM results, regarding properties that are mostly affected by the role of large-scale synoptic conditions and tracer advection regimes, are more representative for a larger domain compared to the local meteorological and O_3 flux observations. By also forcing the SCM with the ERA5 sea ice fraction, we account for sub-grid scale variability in open water and snow or ice surfaces and a different representation of O_3 dry deposition to these surfaces. However, this 0.25° × 0.25° averaged sea-ice fraction might not be representative for the local footprint of the O_3 flux observations, especially in the marginal ice zone. A detailed footprint analysis of the short-term hourly flux observations would be necessary to distinguish the contribution by ocean and snow/ice-covered surfaces in the marginal ice zone as a function of wind direction. Additionally, the ERA5 forcing data set does not account for leads, melt ponds, and ice ridges, which were commonly observed during spring and summer (Nicolaus et al., 2022; Rabe et al., 2022) and that could lead to potential non-linear effects on surface energy balance and turbulent mixing.

Regarding the SCM-simulated meteorology, our findings confirm many other studies that found that model simulations and reanalysis datasets are typically showing a warm bias over snow-covered surfaces (e.g., Savijärvi, 2014; Sterk et al., 2015; Wang et al., 2019; Tjernström et al., 2021). Most notably, Wang et al. (2019) found that the warm bias of ERA5 increases to +5.4°C for T_{2m} < −25°C over the Arctic sea ice. Here, we find an SCM warm bias of +2.1°C for T_{2m} < −25°C compared to a mean T_{2m} bias of +1.0°C for the entire MOSAiC dataset. ERA5 assimilates RV *Polarstern* weather station data (not used in this study) and soundings, which might explain a large part of this discrepancy with Wang et al. (2019). Graham et al. (2019) found that ERA5 performs best among 5 reanalysis products, especially related to the wind fields for a case study in summer. Here, we find that the wind fields (both speed and direction) are well represented by the SCM and arguably also by the role of nudging to ERA5 above the PBL.

Other results further corroborate the representativeness of the SCM for a larger domain compared to the local observations. For example, the surface O_3 observations show more variability on short timescales compared to the SCM (**Figure 4a**). In the SCM, the variability around the mean daily surface O_3 mixing ratio is 2.3 ppb (2σ), whereas the variability in the surface O_3 observations is 5.8 ppb (2σ). Arguably, this difference in variability includes some measurement uncertainty (Angot et al., 2022a) but can also point to missing local processes in the SCM such as snow ridging causing additional surface roughness (Haapala et al., 2013) and mixing, local chemistry caused by halogen emissions from the snowpack (Grannas et al., 2007; Simpson et al., 2007; Morin et al., 2012) and sea ice (Simpson et al., 2005; Jacobi et al., 2006), or missing temporal variability in surface deposition.

The results presented here provide insight on the observed and simulated variability in O_3 deposition, surface O_3 concentrations and the O_3 budget in the PBL.

Rinke et al. (2021) has shown that the meteorological conditions during MOSAiC were relatively normal even though anomalous conditions occurred, especially related to more frequent storm events from fall to spring. Furthermore, because the overall shape and the major features in the MOSAiC observed O_3 concentrations are similar to the limited previous O_3 observations over the Arctic Ocean (Jacobi et al., 2010, and references therein), we deem the results presented here to be representative for the baseline state of Arctic surface O_3.

By analysing for the first time a year-round dataset of eddy-covariance O_3 flux observations over the Arctic sea ice, we have quantified the removal efficiency by the Arctic sea ice and snow surface over the entire year. Previous studies mostly relied on an indirect evaluation of the representation of the dry deposition mechanism in models using surface O_3 observations (Helmig et al., 2007; Barten et al., 2021). Here, we find a large variability in observation-derived surface resistance (r_c) between 10^3 s m^{-1} and 10^6 s m^{-1}. To what extent this variability can be explained by physical processes, such as wind pumping in snow (Helmig et al., 2007) as opposed to measurement uncertainty due to missing observations in the snowpack, remains an open question. The SCM, which contains an empirical representation of wind pumping (Toyota et al., 2014; Murray et al., 2015), only shows a weak sensitivity of wind speed on O_3 deposition to snow. Here, we find a median r_c of 20,000 s m^{-1}, resulting in an O_3 deposition velocity ($V_{d,O3}$) of 0.005 cm s^{-1}. This result corroborates the findings by Helmig et al. (2007) who determined that the magnitude and variability in simulated surface O_3 concentrations were best represented using a $V_{d,O3}$ between 0.00 and 0.01 cm s^{-1} as already implemented by several modelling studies (Barten et al., 2020; Herrmann et al., 2021; Marelle et al., 2021). However, many atmospheric chemistry and transport models still apply by default a surface resistance that is too low by up to an order of magnitude (Simpson et al., 2012; Hardacre et al., 2015; Falk and Søvde Haslerud, 2019; Swanson et al., 2022), resulting in an overestimation of O_3 removal by the surface.

There is uncertainty as to what degree emissions from the RV *Polarstern* being deposited onto the sea-ice surface may have contaminated the snow surface and altered the natural conditions and behaviour of O_3 deposition. From our current understanding of processes controlling O_3 surface uptake (Clifton et al., 2020), most probably any such contamination effects would have increased the O_3 surface uptake through additional depletion of O_3 with gas and liquid-phase particles in the snowpack interstitial air (Bocquet et al., 2007). Consequently, results from the observations reported here, despite being about the lowest surface O_3 uptake rates ever determined, would most likely represent upper threshold values.

The largest discrepancy between the observed and SCM-simulated O_3 concentrations was found in March to the beginning of May when the observations showed ODEs at the surface (**Figure 4a**) also affecting O_3 concentrations above the estimated PBL height (**Figure 5b** and **c**). The SCM does not represent these ODEs, given that we have not considered the role of springtime snowpack and sea-ice emissions of halogens and NO_x in this analysis due to missing observations to constrain these events. Therefore, we deem the results of the SCM PBL O_3 budget as not representative of the spring ODEs for which we would expect a larger contribution by chemistry and recovery of O_3 from turbulent mixing and entrainment of O_3-rich air. An analysis of the multi-year (2003–2021) CAMS O_3 data used to nudge the SCM above the PBL indicates that CAMS also does not show ODEs in spring. Therefore, constraining the SCM with overestimated O_3 concentrations does not provide a realistic representation of the conditions of relevance for the simulation of these ODEs, even if the surface halogen sources would be represented accurately. A detailed analysis of the ODEs and relevant halogen sources should rely on a high resolution regional 3D model simulation, including reactive halogen production due to blowing snow, sea salt aerosols and other sources (Marelle et al., 2021). Alternatively, ODEs could be further assessed with halogen-O_3 chemistry box model experiments being constrained with MOSAiC meteorological and tracer observations.

This study arrives for the first time at a quantification of the PBL O_3 budget over Arctic sea ice and specifically the role of dry deposition in the PBL O_3 budget. We show that dry deposition can strongly affect O_3 concentration in the PBL, especially during events with a shallow boundary layer, even though the O_3 dry deposition velocity to the Arctic sea ice is small compared to any other natural surface (Hardacre et al., 2015). A detailed analysis of the O_3 flux observations, including the potential role of bidirectional exchange and a comparison with other flux observations of CO_2, CH_4 and DMS, is planned for a future manuscript. Such an analysis of flux observations and footprints in combination with ocean water iodide observations might provide insight on the contribution of O_3 deposition to the ocean surface during MOSAiC. However, such an analysis will be limited to individual events when the footprint is dominantly over open ocean and is not expected to influence the results of this study. Furthermore, presence of fresh meltwater on top of the saline ocean (Rabe et al., 2022) during spring and summer might limit the atmosphere-ocean exchange of trace gases. Given the findings that dry deposition to the Arctic sea ice is an important removal mechanism of PBL O_3, a reconsideration of the dry deposition routines and corresponding surface resistance in global and regional atmospheric chemistry and transport models or reanalysis datasets is recommended. This study now confirms based on this one-year O_3 flux dataset that these models overestimate O_3 deposition to snow and ice (Simpson et al., 2012; Hardacre et al., 2015; Falk and Søvde Haslerud, 2019; Barten et al., 2021), likely resulting in an underestimation of Arctic surface and PBL O_3 concentrations. For example, Barten et al. (2021) found a mean underestimation of 5.0 ppb for the CAMS reanalysis product at 6 High Arctic sites (>70°N) for an end-of-summer case, indicating a potential overestimation of the surface removal in shallow boundary layers. Furthermore, the anticipated increase of local air pollution (Law et al., 2017; Schmale

et al., 2018) and shipping emissions (Aliabadi et al., 2015; Stephenson et al., 2018) calls for continuing efforts to enhance our understanding of current estimates of O_3 radiative forcing and the fate of O_3 in the Arctic PBL.

5. Conclusion

This study highlights the role of dry deposition in the O_3 budget of the Planetary Boundary Layer (PBL) over the Arctic sea ice. We quantified the removal of O_3 by dry deposition to sea-ice and snow-covered surfaces using, for the first time, year-round O_3 flux observations in the High Arctic as part of MOSAiC campaign. By combining this information with model simulations using a single-column atmospheric chemistry and meteorological model, we quantified the role of deposition and other processes in determining the O_3 concentration in the PBL.

The SCM-simulated meteorology shows a good resemblance with observations, having an R^2 of 0.88, 0.84 and 0.85 for 2-m air temperature (T_{2m}), 10-m wind speed (V_{10m}) and 10-m wind direction, respectively. On average, the SCM is unbiased with respect to wind direction and V_{10m}. However, the SCM shows a warm bias for T_{2m}, being on average $+1.0°C$ and increasing to $+2.1°C$ for $T_{2m} < -25°C$, related to an underestimation of the stable stratification at the surface. The SCM-simulated meteorology is also strongly affected by nudging to ERA5 above the boundary layer. The SCM-simulated PBL Height (PBLH) agrees well with radiosonde-derived PBLH in terms of temporal variability and identification of extended periods, with shallow boundary layers and limited mixing during calm conditions essential for the fate of O_3 in the PBL.

From the eddy-covariance O_3 flux observations we infer the O_3 deposition surface resistance (r_c) as a residual term by calculating the aerodynamic resistance (r_a) and quasi-laminar sub-layer resistance (r_b) based on the stability of the atmosphere. We find that r_a, representing turbulent transport to the surface, is on the order of 10^2 s m^{-1}. Diffusion close to the surface, reflected by r_b, is typically one order of magnitude smaller (10^1 s m^{-1}) than r_a. A high temporal variability in observation-derived r_c was found, ranging between 10^3 s m^{-1} and 10^6 s m^{-1}. Applying a 7-day running median to derive the long-term r_c relevant for the PBL O_3 budget results in an r_c of 20,000 s m^{-1} ($V_{d,O3} \asymp 0.005$ cm s^{-1}). This value is among the lowest surface O_3 uptake ever determined and most likely represents upper threshold values, given potential contamination effects. Over the whole year, the total removal rate of O_3 to the surface is determined by the uptake efficiency of the snow and ice surface, because turbulent transport to the surface and diffusion close to the surface are seldom a limiting factor for O_3 deposition in this study.

The SCM is able to represent the yearly cycle in observed surface O_3 related to the wintertime maximum of >40 ppb and the end-of-summer minimum of approximately 15 ppb. However, the SCM is unable to reproduce the ODEs in spring due to missing halogen sources in the model and in the CAMS reanalysis dataset that was used to nudge the model. In wintertime, the PBL O_3 budget is governed mainly by removal of O_3 at the surface by dry deposition compensated by downward turbulent transport, with weekly mean tendencies up to 0.25 ppb h^{-1}. In summer, advection, which is accounted for implicitly by nudging to CAMS, also poses a significant mostly negative contribution to the PBL O_3 budget that is typically larger than the removal of O_3 by dry deposition. The contribution by dry deposition strongly depends on the depth of the PBL. During extended periods with low wind speeds ($V_{10m} < 5$ m s^{-1}) and shallow boundary layers (<50 m), the weekly mean removal tendency of O_3 by dry deposition can reach up to -1.0 ppb h^{-1}. Entrainment and the net effect of chemistry only contribute marginally (<5%) to the total simulated PBL O_3 budget.

By including vertical O_3 concentration profiles collected by 56 O_3 sondes, we gain insight on the vertical structure of PBL and free tropospheric O_3. In wintertime, we find weak O_3 gradients from the surface to the free troposphere. In springtime, the observed profiles indicate that depleted O_3 concentrations caused by the ODEs are limited to a few hundreds of meters above the PBL, resulting in very sharp vertical O_3 gradients. In the end-of-summer period, strong vertical O_3 gradients are caused by depleted O_3 concentrations in the PBL and limited entrainment of free tropospheric air with enhanced O_3 concentrations.

Results of this study strongly motivate a revision of the representation of sea ice and snow deposition of O_3 in global and regional atmospheric chemistry models, especially because many models still use surface resistances for snow and ice surfaces up to an order of magnitude smaller than presented here. Improved representations of deposition will yield better simulations of Arctic air quality, especially during calm conditions with very shallow PBLs when dry deposition strongly affects boundary layer O_3 concentrations. They also provide improved constraints on the removal role of snow and ice in the total tropospheric O_3 budget and O_3 burden in current and future climate.

Data accessibility statement

Single-column atmospheric chemistry and meteorological model: The model code and output files for the one year MOSAiC simulations are available through Barten and Ganzeveld (2022): https://doi.org/10.5281/zenodo.6546452.

ERA5 reanalysis: Available through the Climate Data Store (CDS) https://cds.climate.copernicus.eu/.

CAMS reanalysis: Available through the Atmosphere Data Store (ADS) https://ads.atmosphere.copernicus.eu/.

Ozone fluxes: Available through Blomquist et al. (2022): http://arcticdata.io/data/10.18739/A2NC5SD71.

Ambient ozone concentrations: Available through Angot et al. (2022b): https://doi.pangaea.de/10.1594/PANGAEA.944393. Based on measurements from https://doi.org/10.5439/1346692, https://doi.org/10.18739/A2736M36B and https://doi.pangaea.de/10.1594/PANGAEA.944268.

Radiosondes: Available through Maturilli et al. (2021): https://doi.pangaea.de/10.1594/PANGAEA.928656.

Ozone sondes: Data for leg 1, 2 and 3 is available through von der Gathen and Maturilli (2020): https://

doi.org/10.1594/PANGAEA.919538. Data for leg 4 and 5 is available through von der Gathen and Maturilli (2022): https://doi.org/10.1594/PANGAEA.941294.

Meteorological data: Available through Cox et al. (2021): http://dx.doi.org/10.18739/A20C4SM1J.

Supplemental files

The supplemental files for this article can be found as follows:

Figure S1. Role of ERA5 in nudging the SCM.

Figure S2. Role of CAMS in nudging the SCM.

Acknowledgments

Data used in this manuscript were produced as part of the international Multidisciplinary drifting Observatory for the Study of the Arctic Climate (MOSAiC) with the tag MOSAiC20192020. We acknowledge everyone involved in the RV *Polarstern* expedition (AWI_PS122_00) for collection and accessibility of the observations (Nixdorf et al., 2021). Some ozone observations were made by the Atmospheric Radiation Measurement (ARM) User Facility, a U.S. Department of Energy Office of Science User Facility Managed by the Biological and Environmental Research Program. We acknowledge the editors and reviewers for their time and effort in reviewing this manuscript. Their suggestions and comments have greatly helped in improving the content and readability of this manuscript.

Funding

JGMB has been supported by the Nederlandse Organisatie voor Wetenschappelijk Onderzoek (grant no. 866.18.004). Ozone flux measurements were funded by the U.S. National Science Foundation (awards OPP-1807496, OPP-1914781, and OPP-1807163). We acknowledge funding from the Swiss National Sciences Foundation (grant no. 188478) and the Swiss Polar Institute for measurements in the Swiss Container. JS holds the Ingvar Kamprad Chair for Extreme Environments Research. Meteorological data were supported by the U.S. National Science Foundation (OPP-1724551) and the NOAA Physical Sciences Laboratory.

Competing interests

Detlev Helmig serves as one of the Editors-in-Chief for *Elementa: Science of the Anthropocene*. Byron Blomquist serves as an Associate Editor of the *Elementa Atmospheric Sciences Domain*. Matthew Shupe serves as one of the guest editors for the special issue *The Multidisciplinary Drifting Observatory for the Study of Arctic Climate (MOSAiC)* published in Elementa. None of the previously mentioned co-authors was involved in the review process of this manuscript. The authors report no other competing interests.

Author contributions

Design of the study: JGMB, LNG, and GJS.

Model simulations, analysis and interpretation: JGMB.

Ozone flux observations: BWB, HA, SDA, LB, DHe, DHo, JH, HWJ, and KMP.

Ambient ozone observations: HA, BWB, DHo, SDA, LB, IB, DHe, JH, HWJ, TJ, TL, KMP, LQ, MDS, JS, and MB.

Ozonesonde observations: PvdG.

Meteorological measurements: MDS.

All authors contributed to writing of the manuscript and approved submission of the manuscript.

References

Ainsworth, EA, **Yendrek, CR**, **Sitch, S**, **Collins, WJ**, **Emberson, LD.** 2012. The effects of tropospheric ozone on net primary productivity and implications for climate change. *Annual Review of Plant Biology* **63**: 637–661. DOI: http://dx.doi.org/10.1146/annurev-arplant-042110-103829.

Aliabadi, AA, **Staebler, RM**, **Sharma, S.** 2015. Air quality monitoring in communities of the Canadian Arctic during the high shipping season with a focus on local and marine pollution. *Atmospheric Chemistry and Physics* **15**(5): 2651–2673. DOI: http://dx.doi.org/10.5194/acp-15-2651-2015.

Angot, H, **Blomquist, B**, **Howard, D**, **Archer, S**, **Bariteau, L**, **Beck, I**, **Boyer, M**, **Crotwell, M**, **Helmig, D**, **Hueber, J**, **Jacobi, H-W**, **Jokinen, T**, **Kulmala, M**, **Lan, X**, **Laurila, T**, **Madronich, M**, **Neff, D**, **Petäjä, T**, **Posman, K**, **Quéléver, L**, **Shupe, MD**, **Vimont, I**, **Schmale, J.** 2022a. Year-round trace gas measurements in the central Arctic during the MOSAiC expedition. *Scientific Data* **9**(1): 1–19.

Angot, H, **Blomquist, B**, **Howard, D**, **Archer, S**, **Bariteau, L**, **Beck, I**, **Helmig, D**, **Hueber, J**, **Jacobi, H-W**, **Jokinen, T**, **Laurila, T**, **Posman, K**, **Quéléver, L**, **Shupe, MD**, **Schmale, J**, **Boyer, M.** 2022b. Ozone dry air mole fractions measured during MOSAiC 2019/2020 (merged dataset). *PANGAEA*. DOI: https://doi.pangaea.de/10.1594/PANGAEA.944393.

Bariteau, L, **Helmig, D**, **Fairall, CW**, **Hare, JE**, **Hueber, J**, **Lang, EK.** 2010. Determination of oceanic ozone deposition by ship-borne eddy covariance flux measurements. *Atmospheric Measurement Techniques* **3**(2): 441–455. DOI: http://dx.doi.org/10.5194/amt-3-441-2010.

Barten, JGM, **Ganzeveld, LN.** 2022. Single-column atmospheric chemistry and meteorological model simulations for MOSAiC. DOI: http://dx.doi.org/10.5281/zenodo.6546452.

Barten, JGM, **Ganzeveld, LN, Steeneveld, G-J, Krol, MC.** 2021**.** Role of oceanic ozone deposition in explaining temporal variability in surface ozone at High Arctic sites. *Atmospheric Chemistry and Physics* **21**(13): 10229–10248. DOI: http://dx.doi.org/10.5194/acp-21-10229-2021.

Barten, JGM, **Ganzeveld, LN**, **Visser, AJ**, **Jiménez, R**, **Krol, MC.** 2020. Evaluation of nitrogen oxides (NO_x) sources and sinks and ozone production in Colombia and surrounding areas. *Atmospheric Chemistry and Physics* **20**(15): 9441–9458. DOI: http://dx.doi.org/10.5194/acp-20-9441-2020.

Basu, S, **Holtslag, AAM**, **Caporaso, L**, **Riccio, A**, **Steeneveld, G-J.** 2014. Observational support for the

stability dependence of the bulk Richardson number across the stable boundary layer. *Boundary-Layer Meteorology* **150**(3): 515–523. DOI: http://dx.doi.org/10.1007/s10546-013-9878-y.

Beck, I, **Angot, H**, **Baccarini, A**, **Dada, L**, **Quéléver, L**, **Jokinen, T**, **Laurila, T**, **Lampimäki, M**, **Bukowiecki, N**, **Boyer, M**, **Gong, X**, **Gysel-Beer, M**, **Petäjä, T**, **Wang, J**, **Schmale, J.** 2022. Automated identification of local contamination in remote atmospheric composition time series. *Atmospheric Measurement Techniques* **15**(14): 4195–4224. DOI: http://dx.doi.org/10.5194/amt-15-4195-2022.

Berkowitz, CM, **Fast, JD**, **Easter, RC.** 2000. Boundary layer vertical exchange processes and the mass budget of ozone: Observations and model results. *Journal of Geophysical Research: Atmospheres* **105**(D11): 14789–14805. DOI: http://dx.doi.org/10.1029/2000JD900026.

Blomquist, BW, **Helmig, D**, **Archer, SD**, **Ganzeveld, LN**, **Howard, D**, **Angot, H**, **Bariteau, L**, **Jacobi, H-W**, **Posman, KM**, **Hueber, J.** 2022. Trace gas and wind velocities at 10 Hertz from Research Vessel Polarstern bow tower during the MOSAiC Arctic drift campaign, 2019–2020. Arctic Data Center. Available at http://arcticdata.io/data/10.18739/A2NC5SD71.

Blomquist, BW, **Huebert, BJ**, **Fairall, CW**, **Bariteau, L**, **Edson, JB**, **Hare, JE**, **McGillis, WR.** 2014. Advances in air-sea CO_2 flux measurement by eddy correlation. *Boundary-Layer Meteorology* **152**(3): 245–276. DOI: http://dx.doi.org/10.1007/s10546-014-9926-2.

Blomquist, BW, **Huebert, BJ**, **Fairall, CW**, **Faloona, IC.** 2010. Determining the sea-air flux of dimethylsulfide by eddy correlation using mass spectrometry. *Atmospheric Measurement Techniques* **3**(1): 1–20. DOI: http://dx.doi.org/10.5194/amt-3-1-2010.

Bocquet, F, **Helmig, D**, **Oltmans, SJ.** 2007. Ozone in interstitial air of the mid-latitude, seasonal snowpack at Niwot Ridge, Colorado. *Arctic, Antarctic, and Alpine Research* **39**(3): 375–387. DOI: http://dx.doi.org/10.1657/1523-0430(06-027)[BOQUET]2.0.CO;2.

Boylan, P, **Helmig, D**, **Park, J-H.** 2014. Characterization and mitigation of water vapor effects in the measurement of ozone by chemiluminescence with nitric oxide. *Atmospheric Measurement Techniques* **7**(5): 1231–1244. DOI: http://dx.doi.org/10.5194/amt-7-1231-2014.

Brooks, IM, **Tjernström, M**, **Persson, POG**, **Shupe, MD**, **Atkinson, RA**, **Canut, G**, **Birch, CE**, **Mauritsen, T**, **Sedlar, J**, **Brooks, BJ.** 2017. The turbulent structure of the Arctic summer boundary layer during the Arctic Summer Cloud-Ocean Study. *Journal of Geophysical Research: Atmospheres* **122**(18): 9685–9704. DOI: http://dx.doi.org/10.1002/2017JD027234.

Carminati, F, **Migliorini, S**, **Ingleby, B**, **Bell, W**, **Lawrence, H**, **Newman, S**, **Hocking, J**, **Smith, A.** 2019. Using reference radiosondes to characterise NWP model uncertainty for improved satellite calibration and validation. *Atmospheric Measurement Techniques* **12**(1): 83–106. DOI: http://dx.doi.org/10.5194/amt-12-83-2019.

Chen, X, **Quéléver, LLJ**, **Fung, PL**, **Kesti, J**, **Rissanen, MP**, **Bäck, J**, **Keronen, P**, **Junninen, H**, **Petäjä, T**, **Kerminen, V-M**, **Kulmala, M.** 2018. Observations of ozone depletion events in a Finnish boreal forest. *Atmospheric Chemistry and Physics* **18**(1): 49–63. DOI: http://dx.doi.org/10.5194/acp-18-49-2018.

Clifton, OE, **Fiore, AM**, **Massman, WJ**, **Baublitz, CB**, **Coyle, M**, **Emberson, L**, **Fares, S**, **Farmer, DK**, **Gentine, P**, **Gerosa, G**, **Guenther, AB**, **Helmig, D**, **Lombardozzi, DL**, **Munger, JW**, **Patton, EG**, **Pusede, SE**, **Schwede, DB**, **Silva, SJ**, **Sörgel, M**, **Steiner, AL**, **Tai, APK.** 2020. Dry deposition of ozone over land: Processes, measurement, and modeling. *Reviews of Geophysics* **58**(1): e2019RG000670. DOI: http://dx.doi.org/10.1029/2019RG000670.

Conley, SA, **Faloona, IC**, **Lenschow, DH**, **Campos, T**, **Heizer, C**, **Weinheimer, A**, **Cantrell, CA**, **Mauldin, RL**, **Hornbrook, RS**, **Pollack, I**, **Bandy, A.** 2011. A complete dynamical ozone budget measured in the tropical marine boundary layer during PASE. *Journal of Atmospheric Chemistry* **68**(1): 55–70. DOI: http://dx.doi.org/10.1007/s10874-011-9195-0.

Cooper, OR, **Parrish, DD**, **Ziemke, J**, **Balashov, NV**, **Cupeiro, M**, **Galbally, IE**, **Gilge, S**, **Horowitz, L**, **Jensen, NR**, **Lamarque, J-F**, **Naik, V**, **Oltmans, SJ**, **Schwab, J**, **Shindell, DT**, **Thompson, AM**, **Thouret, V**, **Wang, Y**, **Zbinden, RM.** 2014. Global distribution and trends of tropospheric ozone: An observation-based review. *Elementa: Science of the Anthropocene* **2**: 000029. DOI: http://dx.doi.org/10.12952/journal.elementa.000029.

Cooper, OR, **Schultz, MG**, **Schröder, S**, **Chang, K-L**, **Gaudel, A**, **Carbajal-Bentez, G**, **Cuevas, E**, **Fröhlich, M**, **Galbally, IE**, **Molloy, S**, **Kubistin, D**, **Lu, X**, **McClure-Begley, A**, **Nédélec, P**, **O'Brien, J**, **Oltmans, SJ**, **Petropavlovskikh, I**, **Ries, L**, **Senik, I**, **Sjöberg, K**, **Solberg, S**, **Spain, GT**, **Spangl, W**, **Steinbacher, M**, **Tarasick, D**, **Thouret, V**, **Xu, X.** 2020. Multi-decadal surface ozone trends at globally distributed remote locations. *Elementa: Science of the Anthropocene* **8**: 23. DOI: http://dx.doi.org/10.1525/elementa.420.

Cox, C, **Gallagher, M**, **Shupe, M**, **Persson, O**, **Solomon, A**, **Ayers, T**, **Costa, D**, **Hutchings, J**, **Leach, J**, **Morris, S**, **Osborn, J**, **Pezoa, S**, **Uttal, T.** 2021. Atmospheric Surface Flux Station #30 measurements (Level 1 Raw), Multidisciplinary Drifting Observatory for the Study of Arctic Climate (MOSAiC), central Arctic, October 2019–September 2020. Arctic Data Center. DOI: http://dx.doi.org/10.18739/A20C4SM1J.

Cros, B, **Delon, C**, **Affre, C**, **Marion, T**, **Druilhet, A**, **Perros, PE**, **Lopez, A.** 2000. Sources and sinks of ozone in savanna and forest areas during EXPRESSO: Airborne turbulent flux measurements. *Journal of Geophysical Research: Atmospheres* **105**(D24):

29347–29358. DOI: http://dx.doi.org/10.1029/2000JD900451.

de Jalón, SG, **Burgess, PJ**, **Curiel Yuste, J**, **Moreno, G**, **Graves, A**, **Palma, JHN**, **Crous-Duran, J**, **Kay, S**, **Chiabai, A.** 2019. Dry deposition of air pollutants on trees at regional scale: A case study in the Basque Country. *Agricultural and Forest Meteorology* **278**: 107648. DOI: http://dx.doi.org/10.1016/j.agrformet.2019.107648.

Fairall, CW, **Yang, M**, **Bariteau, L**, **Edson, JB**, **Helmig, D**, **McGillis, W**, **Pezoa, S**, **Hare, JE**, **Huebert, B**, **Blomquist, B.** 2011. Implementation of the Coupled Ocean-Atmosphere Response Experiment flux algorithm with CO_2, dimethyl sulfide, and O_3. *Journal of Geophysical Research: Oceans* **116**(C4): C00F09. DOI: http://dx.doi.org/10.1029/2010JC006884.

Falk, S, **Sinnhuber, B-M.** 2018. Polar boundary layer bromine explosion and ozone depletion events in the chemistry–climate model EMAC v2.52: Implementation and evaluation of AirSnow algorithm. *Geoscientific Model Development* **11**(3): 1115–1131. DOI: http://dx.doi.org/10.5194/gmd-11-1115-2018.

Falk, S, **Søvde Haslerud, A.** 2019. Update and evaluation of the ozone dry deposition in Oslo CTM3 v1.0. *Geoscientific Model Development* **12**(11): 4705–4728. DOI: http://dx.doi.org/10.5194/gmd-12-4705-2019.

Ganzeveld, LN, **Eerdekens, G**, **Feig, G**, **Fischer, H**, **Harder, H**, **Königstedt, R**, **Kubistin, D, Martinez, M, Meixner, FX, Scheeren, HA**, **Sinha, V**, **Taraborrelli, D**, **Williams, J**, **Vilà-Guerau de Arellano, J**, **Lelieveld, J.** 2008. Surface and boundary layer exchanges of volatile organic compounds, nitrogen oxides and ozone during the GABRIEL campaign. *Atmospheric Chemistry and Physics* **8**(20): 6223–6243. DOI: http://dx.doi.org/10.5194/acp-8-6223-2008.

Ganzeveld, LN, **Klemm, O**, **Rappenglück, B**, **Valverde-Canossa, J.** 2006. Evaluation of meteorological parameters over a coniferous forest in a single-column chemistry-climate model. *Atmospheric Environment* **40**: 21–27. DOI: http://dx.doi.org/10.1016/j.atmosenv.2006.01.061.

Ganzeveld, LN, **Lelieveld, J.** 1995. Dry deposition parameterization in a chemistry general circulation model and its influence on the distribution of reactive trace gases. *Journal of Geophysical Research: Atmospheres* **100**(D10): 20999–21012. DOI: http://dx.doi.org/10.1029/95JD02266.

Ganzeveld, LN, **Lelieveld, J**, **Dentener, FJ**, **Krol, MC**, **Roelofs, G-J.** 2002. Atmosphere-biosphere trace gas exchanges simulated with a single-column model. *Journal of Geophysical Research: Atmospheres* **107**(D16): ACH–8. DOI: http://dx.doi.org/10.1029/2001JD000684.

Graham, RM, **Cohen, L**, **Ritzhaupt, N**, **Segger, B**, **Graversen, RG**, **Rinke, A**, **Walden, VP**, **Granskog, MA**, **Hudson, SR.** 2019. Evaluation of six atmospheric reanalyses over Arctic sea ice from winter to early summer. *Journal of Climate* **32**(14): 4121–4143. DOI: http://dx.doi.org/10.1175/JCLI-D-18-0643.1.

Grannas, AM, **Jones, AE**, **Dibb, J**, **Ammann, M**, **Anastasio, C**, **Beine, H**, **Bergin, M**, **Bottenheim, J**, **Boxe, C**, **Carver, G**, **Chen, G**, **Crawford, JH**, **Dominé, F**, **Frey, MM**, **Guzmán, MI**, **Heard, DE**, **Helmig, D**, **Hoffmann, MR**, **Honrath, RE**, **Huey, LG**, **Hutterli, M**, **Jacobi, HW**, **Klán, P**, **Lefer, B**, **McConnell, J**, **Plane, J**, **Sander, R**, **Savarino, J**, **Shepson, PB**, **Simpson, WR**, **Sodeau, JR**, **von Glasow, R**, **Weller, R**, **Wolff, EW**, **Zhu, T.** 2007. An overview of snow photochemistry: Evidence, mechanisms and impacts. *Atmospheric Chemistry and Physics* **7**(16): 4329–4373. DOI: http://dx.doi.org/10.5194/acp-7-4329-2007.

Haapala, J, **Lensu, M**, **Dumont, M**, **Renner, AHH**, **Granskog, MA**, **Gerland, S.** 2013. Small-scale horizontal variability of snow, sea-ice thickness and freeboard in the first-year ice region north of Svalbard. *Annals of Glaciology* **54**(62): 261–266. DOI: http://dx.doi.org/10.3189/2013AoG62A157.

Hardacre, C, **Wild, O**, **Emberson, L.** 2015. An evaluation of ozone dry deposition in global scale chemistry climate models. *Atmospheric Chemistry and Physics* **15**(11): 6419–6436. DOI: http://dx.doi.org/10.5194/acp-15-6419-2015.

Helmig, D, **Bocquet, F**, **Cohen, L**, **Oltmans, SJ.** 2007. Ozone uptake to the polar snowpack at Summit, Greenland. *Atmospheric Environment* **41**(24): 5061–5076. DOI: http://dx.doi.org/10.1016/j.atmosenv.2006.06.064.

Helmig, D, **Ganzeveld, L**, **Butler, T**, **Oltmans, SJ.** 2007. The role of ozone atmosphere-snow gas exchange on polar, boundary-layer tropospheric ozone—A review and sensitivity analysis. *Atmospheric Chemistry and Physics* **7**(1): 15–30. DOI: http://dx.doi.org/10.5194/acp-7-15-2007.

Herrmann, M, **Sihler, H**, **Frieß, U**, **Wagner, T**, **Platt, U**, **Gutheil, E.** 2021. Time-dependent 3D simulations of tropospheric ozone depletion events in the Arctic spring using the Weather Research and Forecasting model coupled with Chemistry (WRF-Chem). *Atmospheric Chemistry and Physics* **21**(10): 7611–7638. DOI: http://dx.doi.org/10.5194/acp-21-7611-2021.

Hersbach, H, **Bell, B**, **Berrisford, P**, **Hirahara, S**, **Horányi, A**, **Muñoz-Sabater, J**, **Nicolas, J**, **Peubey, C**, **Radu, R**, **Schepers, D**, **Simmons, A**, **Soci, C**, **Abdalla, S**, **Abellan, X**, **Balsamo, G**, **Bechtold, P**, **Biavati, G**, **Bidlot, J**, **Bonavita, M**, **De Chiara, G**, **Dahlgren, P**, **Dee, D**, **Diamantakis, M**, **Dragani, R**, **Flemming, J**, **Forbes, R**, **Fuentes, M**, **Geer, A**, **Haimberger, L**, **Healy, S**, **Hogan, RJ**, **Hólm, E**, **Janisková, M**, **Keeley, S**, **Laloyaux, P**, **Lopez, P**, **Lupu, C**, **Radnoti, G**, **de Rosnay, P**, **Rozum, I**, **Vamborg, F**, **Villaume, S**, **Thépaut, JN.** 2020. The ERA5 global reanalysis. *Quarterly Journal of the Royal Meteorological Society* **146**(730): 1999–2049. DOI: http://dx.doi.org/10.1002/qj.3803.

Hicks, BB, **Baldocchi, DD**, **Meyers, TP**, **Hosker, RP**, **Matt, DR.** 1987. A preliminary multiple resistance routine

for deriving dry deposition velocities from measured quantities. *Water, Air, and Soil Pollution* **36**(3–4): 311–330. DOI: http://dx.doi.org/10.1007/BF00229675.

Hou, X, **Zhu, B**, **Fei, D**, **Wang, D.** 2015. The impacts of summer monsoons on the ozone budget of the atmospheric boundary layer of the Asia-Pacific region. *Science of the Total Environment* **502**: 641–649. DOI: http://dx.doi.org/10.1016/j.scitotenv.2014.09.075.

Inness, A, **Ades, M**, **Agust-Panareda, A**, **Barré, J**, **Benedictow, A**, **Blechschmidt, A-M**, **Dominguez, JJ**, **Engelen, R**, **Eskes, H**, **Flemming, J**, **Huijnen, V**, **Jones, L**, **Kipling, Z**, **Massart, S**, **Parrington, M**, **Peuch, VH**, **Razinger, M**, **Remy, S**, **Schulz, M**, **Suttie, M.** 2019. The CAMS reanalysis of atmospheric composition. *Atmospheric Chemistry and Physics* **19**(6): 3515–3556. DOI: http://dx.doi.org/10.5194/acp-19-3515-2019.

Inness, A, **Chabrillat, S**, **Flemming, J**, **Huijnen, V**, **Langenrock, B**, **Nicolas, J**, **Polichtchouk, I**, **Razinger, M.** 2020. Exceptionally low Arctic stratospheric ozone in spring 2020 as seen in the CAMS reanalysis. *Journal of Geophysical Research: Atmospheres* **125**(23): e2020JD033563. DOI: http://dx.doi.org/10.1029/2020JD033563.

Jacobi, H-W, **Kaleschke, L**, **Richter, A**, **Rozanov, A**, **Burrows, JP.** 2006. Observation of a fast ozone loss in the marginal ice zone of the Arctic Ocean. *Journal of Geophysical Research: Atmospheres* **111**(D15): D15309. DOI: http://dx.doi.org/10.1029/2005JD006715.

Jacobi, H-W, **Morin, S**, **Bottenheim, JW.** 2010. Observation of widespread depletion of ozone in the springtime boundary layer of the central Arctic linked to mesoscale synoptic conditions. *Journal of Geophysical Research: Atmospheres* **115**(D17): D17302. DOI: http://dx.doi.org/10.1029/2010JD013940.

Jozef, G, **Cassano, J**, **Dahlke, S**, **de Boer, G.** 2022. Testing the efficacy of atmospheric boundary layer height detection algorithms using uncrewed aircraft system data from MOSAiC. *Atmospheric Measurement Techniques* **15**(13): 4001–4022. DOI: http://dx.doi.org/10.5194/amt-15-4001-2022.

Keen, A, **Blockley, E.** 2018. Investigating future changes in the volume budget of the Arctic sea ice in a coupled climate model. *The Cryosphere* **12**(9): 2855–2868. DOI: http://dx.doi.org/10.5194/tc-12-2855-2018.

Kral, ST, **Reuder, J**, **Vihma, T**, **Suomi, I**, **Haualand, KF**, **Urbancic, GH**, **Greene, BR**, **Steeneveld, G-J**, **Lorenz, T**, **Maronga, B**, **Jonassen, MO**, **Ajosenpää, H**, **Båserud, L**, **Chilson, PB**, **Holtslag, AAM**, **Jenkins, AD**, **Kouznetsov, R**, **Mayer, S**, **Pillar-Little, EA**, **Rautenberg, A**, **Schwenkel, J**, **Seidl, AW**, **Wrenger, B.** 2021. The innovative strategies for observations in the Arctic Atmospheric Boundary Layer Project (ISOBAR): Unique finescale observations under stable and very stable conditions. *Bulletin of the American Meteorological Society* **102**(2): E218–E243. DOI: http://dx.doi.org/10.1175/BAMS-D-19-0212.1.

Kuhn, U, **Ganzeveld, L**, **Thielmann, A**, **Dindorf, T**, **Schebeske, G**, **Welling, M**, **Sciare, J**, **Roberts, G**, **Meixner, FX**, **Kesselmeier, J**, **Lelieveld, J**, **Kolle, O**, **Ciccioli, P**, **Lloyd, J**, **Trentmann, J**, **Artaxo, P**, **Andreae, MO.** 2010. Impact of Manaus City on the Amazon Green Ocean atmosphere: Ozone production, precursor sensitivity and aerosol load. *Atmospheric Chemistry and Physics* **10**(19): 9251–9282. DOI: http://dx.doi.org/10.5194/acp-10-9251-2010.

Law, KS, **Roiger, A**, **Thomas, JL**, **Marelle, L**, **Raut, J-C**, **Dalsøren, S**, **Fuglestvedt, J**, **Tuccella, P**, **Weinzierl, B**, **Schlager, H.** 2017. Local Arctic air pollution: Sources and impacts. *Ambio* **46**(S3): 453–463. DOI: http://dx.doi.org/10.1007/s13280-017-0962-2.

Lei, R, **Cheng, B**, **Hoppmann, M**, **Zuo, G.** 2021. Snow depth and sea ice thickness derived from the measurements of SIMBA buoy 2019T69. PANGAEA. DOI: http://dx.doi.org/10.1594/PANGAEA.938235.

Lelieveld, J, **Dentener, FJ.** 2000. What controls tropospheric ozone? *Journal of Geophysical Research: Atmospheres* **105**(D3): 3531–3551. DOI: http://dx.doi.org/10.1029/1999JD901011.

Lin, M, **Holloway, T**, **Oki, T**, **Streets, DG**, **Richter, A.** 2009. Multi-scale model analysis of boundary layer ozone over East Asia. *Atmospheric Chemistry and Physics* **9**(10): 3277–3301. DOI: http://dx.doi.org/10.5194/acp-9-3277-2009.

Loades, DC, **Yang, M**, **Bell, TG**, **Vaughan, AR**, **Pound, RJ**, **Metzger, S**, **Lee, JD**, **Carpenter, LJ.** 2020. Ozone deposition to a coastal sea: Comparison of eddy covariance observations with reactive air–sea exchange models. *Atmospheric Measurement Techniques* **13**(12): 6915–6931. DOI: http://dx.doi.org/10.5194/amt-13-6915-2020.

Lu, X, **Zhang, L**, **Shen, L.** 2019. Meteorology and climate influences on tropospheric ozone: A review of natural sources, chemistry, and transport patterns. *Current Pollution Reports* **5**(4): 238–260. DOI: http://dx.doi.org/10.1007/s40726-019-00118-3.

Marelle, L, **Thomas, JL**, **Ahmed, S**, **Tuite, K**, **Stutz, J**, **Dommergue, A**, **Simpson, WR**, **Frey, MM**, **Baladima, F.** 2021. Implementation and impacts of surface and blowing snow sources of Arctic bromine activation within WRF-Chem 4.1.1. *Journal of Advances in Modeling Earth Systems* **13**(8): e2020MS002391. DOI: http://dx.doi.org/10.1029/2020MS002391.

Maturilli, M, **Holdridge, DJ**, **Dahlke, S**, **Graeser, J**, **Sommerfeld, A**, **Jaiser, R**, **Deckelmann, H**, **Schulz, A.** 2021. Initial radiosonde data from 2019-10 to 2020-09 during project MOSAiC. DOI: http://dx.doi.org/10.1594/PANGAEA.928656.

Monks, PS, **Salisbury, G**, **Holland, G**, **Penkett, SA**, **Ayers, GP.** 2000. A seasonal comparison of ozone photochemistry in the remote marine boundary layer. *Atmospheric Environment* **34**(16): 2547–2561. DOI: http://dx.doi.org/10.1016/S1352-2310(99)00504-X.

Morin, S, **Erbland, J**, **Savarino, J**, **Domine, F**, **Bock, J**, **Friess, U**, **Jacobi, H-W**, **Sihler, H**, **Martins, JMF**.

2012. An isotopic view on the connection between photolytic emissions of NO_x from the Arctic snowpack and its oxidation by reactive halogens. *Journal of Geophysical Research: Atmospheres* **117**(D14): D00R08. DOI: http://dx.doi.org/10.1029/2011JD016618.

Murray, KA, **Kramer, LJ**, **Doskey, PV**, **Ganzeveld, L**, **Seok, B**, **Van Dam, B**, **Helmig, D.** 2015. Dynamics of ozone and nitrogen oxides at Summit, Greenland. II. Simulating snowpack chemistry during a spring high ozone event with a 1-D process-scale model. *Atmospheric Environment* **117**: 110–123. DOI: http://dx.doi.org/10.1016/j.atmosenv.2015.07.004.

Nicolaus, M, **Perovich, DK**, **Spreen, G**, **Granskog, MA**, **von Albedyll, L**, **Angelopoulos, M**, **Anhaus, P**, **Arndt, S**, **Belter, HJ**, **Bessonov, V**, **Birnbaum, G**, **Brauchle, J**, **Calmer, R**, **Cardellach, E**, **Cheng, B**, **Clemens-Sewall, D**, **Dadic, R**, **Damm, E**, **de Boer, G**, **Demir, O**, **Dethloff, K**, **Divine, DV**, **Fong, AA**, **Fons, S**, **Frey, MM**, **Fuchs, N**, **Gabarró, C**, **Gerland, S**, **Goessling, HF**, **Gradinger, R**, **Haapala, J**, **Haas, C**, **Hamilton, J**, **Hannula, H-R**, **Hendricks, S**, **Herber, A**, **Heuzé, C**, **Hoppmann, M**, **Høyland, KV**, **Huntemann, M**, **Hutchings, JK**, **Hwang, B**, **Itkin, P**, **Jacobi, H-W**, **Jaggi, M**, **Jutila, A**, **Kaleschke, L**, **Katlein, C**, **Kolabutin, N**, **Krampe, D**, **Kristensen, SS**, **Krumpen, T**, **Kurtz, N**, **Lampert, A**, **Lange, BA**, **Lei, R**, **Light, B**, **Linhardt, F**, **Liston, GE**, **Loose, B**, **Macfarlane, AR**, **Mahmud, M**, **Matero, IO**, **Maus, S**, **Morgenstern, A**, **Naderpour, R**, **Nandan, V**, **Niubom, A**, **Oggier, M**, **Oppelt, N**, **Pätzold, F**, **Perron, C**, **Petrovsky, T**, **Pirazzini, R**, **Polashenski, C**, **Rabe, B**, **Raphael, IA**, **Regnery, J**, **Rex, M**, **Ricker, R**, **Riemann-Campe, K**, **Rinke, A**, **Rohde, J**, **Salganik, E**, **Scharien, RK**, **Schiller, M**, **Schneebeli, M**, **Semmling, M**, **Shimanchuk, E**, **Shupe, MD**, **Smith, MM**, **Smolyanitsky, V**, **Sokolov, V**, **Stanton, T**, **Stroeve, J**, **Thielke, L**, **Timofeeva, A**, **Tonboe, RT**, **Tavri, A**, **Tsamados, M**, **Wagner, DN**, **Watkins, D**, **Webster, M**, **Wendisch, M.** 2022. Overview of the MOSAiC expedition: Snow and sea ice. *Elementa: Science of the Anthropocene* **10**(1): 000046. DOI: http://dx.doi.org/10.1525/elementa.2021.000046.

Nixdorf, U, **Dethloff, K**, **Rex, M**, **Shupe, M**, **Sommerfeld, A**, **Perovich, DK**, **Nicolaus, M**, **Heuzé, C**, **Rabe, B**, **Loose, B**, **Damm, E**, **Gradinger, R**, **Fong, A**, **Maslowski, W**, **Rinke, A**, **Kwok, R**, **Spreen, G**, **Wendisch, M**, **Herber, A**, **Hirsekorn, M**, **Mohaupt, V**, **Frickenhaus, S**, **Immerz, A**, **Weiss-Tuider, K**, **König, B**, **Mengedoht, D**, **Regnery, J**, **Gerchow, P**, **Ransby, D**, **Krumpen, T**, **Morgenstern, A**, **Haas, C**, **Kanzow, T**, **Rack, FR**, **Saitzev, V**, **Sokolov, V**, **Makarov, A**, **Schwarze, S**, **Wunderlich, T**, **Wurr, K**, **Boetius, A.** 2021. MOSAiC extended acknowledgement. DOI: http://dx.doi.org/10.5281/zenodo.5541624.

Nuvolone, D, **Petri, D**, **Voller, F.** 2018. The effects of ozone on human health. *Environmental Science and Pollution Research* **25**(9): 8074–8088. DOI: http://dx.doi.org/10.1007/s11356-017-9239-3.

Rabe, B, **Heuzé, C**, **Regnery, J**, **Aksenov, Y**, **Allerholt, J**, **Athanase, M**, **Bai, Y**, **Basque, C**, **Bauch, D**, **Baumann, TM**, **Chen, D**, **Cole, ST**, **Craw, L**, **Davies, A**, **Damm, E**, **Dethloff, K**, **Divine, DV**, **Doglioni, F**, **Ebert, F**, **Fang, Y-C**, **Fer, I**, **Fong, AA**, **Gradinger, R**, **Granskog, MA**, **Graupner, R**, **Haas, C**, **He, H**, **He, Y**, **Hoppmann, M**, **Janout, M**, **Kadko, D**, **Kanzow, T**, **Karam, S**, **Kawaguchi, Y**, **Koenig, Z**, **Kong, B**, **Krishfield, RA**, **Krumpen, T**, **Kuhlmey, D**, **Kuznetsov, I**, **Lan, M**, **Laukert, G**, **Lei, R**, **Li, T**, **Torres-Valdés, S**, **Lin, L**, **Lin, L**, **Liu, H**, **Liu, N**, **Loose, B**, **Ma, X**, **McKay, R**, **Mallet, M**, **Mallett, RDC**, **Maslowski, W**, **Mertens, C**, **Mohrholz, V**, **Muilwijk, M**, **Nicolaus, M**, **O'Brien, JK**, **Perovich, D**, **Ren, J**, **Rex, M**, **Ribeiro, N**, **Rinke, A**, **Schaffer, J**, **Schuffenhauer, I**, **Schulz, K**, **Shupe, MD**, **Shaw, W**, **Sokolov, V**, **Sommerfeld, A**, **Spreen, G**, **Stanton, T**, **Stephens, M**, **Su, J**, **Sukhikh, N**, **Sundfjord, A**, **Thomisch, K**, **Tippenhauer, S**, **Toole, JM**, **Vredenborg, M**, **Walter, M**, **Wang, H**, **Wang, L**, **Wang, Y**, **Wendisch, M**, **Zhao, J**, **Zhou, M**, **Zhu, J.** 2022. Overview of the MOSAiC expedition: Physical oceanography. *Elementa: Science of the Anthropocene* **10**(1): 00062. DOI: http://dx.doi.org/10.1525/elementa.2021.00062.

Richardson, H, **Basu, S**, **Holtslag, AAM.** 2013. Improving stable boundary-layer height estimation using a stability-dependent critical bulk Richardson number. *Boundary-Layer Meteorology* **148**(1): 93–109. DOI: http://dx.doi.org/10.1007/s10546-013-9812-3.

Rinke, A, **Cassano, JJ**, **Cassano, EN**, **Jaiser, R**, **Handorf, D.** 2021. Meteorological conditions during the MOSAiC expedition: Normal or anomalous? *Elementa: Science of the Anthropocene* **9**(1): 00023. DOI: http://dx.doi.org/10.1525/elementa.2021.00023.

Sander, R, **Kerkweg, A**, **Jöckel, P**, **Lelieveld, J.** 2005. The new comprehensive atmospheric chemistry module MECCA. *Atmospheric Chemistry and Physics* **5**(2): 445–450. DOI: http://dx.doi.org/10.5194/acp-5-445-2005.

Savijärvi, H. 2014. High-resolution simulations of the night-time stable boundary layer over snow. *Quarterly Journal of the Royal Meteorological Society* **140**(680): 1121–1128. DOI: http://dx.doi.org/10.1002/qj.2187.

Schmale, J, **Arnold, SR**, **Law, KS**, **Thorp, T**, **Anenberg, S**, **Simpson, WR**, **Mao, J**, **Pratt, KA.** 2018. Local Arctic air pollution: A neglected but serious problem. *Earth's Future* **6**(10): 1385–1412. DOI: http://dx.doi.org/10.1029/2018EF000952.

Senff, C, **Bösenberg, J**, **Peters, G**, **Schaberl, T.** 1996. Remote sensing of turbulent ozone fluxes and the ozone budget in the convective boundary layer with DIAL and radar-RASS: A case study. *Contributions to Atmospheric Physics* **69**: 161–176.

Seok, B, **Helmig, D**, **Ganzeveld, L**, **Williams, MW**, **Vogel, CS.** 2013. Dynamics of nitrogen oxides and ozone above and within a mixed hardwood forest in northern Michigan. *Atmospheric Chemistry and Physics*

13(15): 7301–7320. DOI: http://dx.doi.org/10.5194/acp-13-7301-2013.

Shupe, MD, **Rex, M**, **Blomquist, B**, **Persson, POG**, **Schmale, J**, **Uttal, T**, **Althausen, D**, **Angot, H**, **Archer, S**, **Bariteau, L**, **Beck, I**, **Bilberry, J**, **Bucci, S**, **Buck, C**, **Boyer, M**, **Brasseur, Z**, **Brooks, IM**, **Calmer, R**, **Cassano, J**, **Castro, V**, **Chu, D**, **Costa, D**, **Cox, CJ**, **Creamean, J**, **Crewell, S**, **Dahlke, S**, **Damm, E**, **de Boer, G**, **Deckelmann, H**, **Dethloff, K**, **Dütsch, M**, **Ebell, K**, **Ehrlich, A**, **Ellis, J**, **Engelmann, R**, **Fong, AA**, **Frey, MM**, **Gallagher, MR**, **Ganzeveld, L**, **Gradinger, R**, **Graeser, J**, **Greenamyer, V**, **Griesche, H**, **Griffiths, S**, **Hamilton, J**, **Heinemann, G**, **Helmig, D**, **Herber, A**, **Heuzé, C**, **Hofer, J**, **Houchens, T**, **Howard, D**, **Inoue, J**, **Jacobi, H-W**, **Jaiser, R**, **Jokinen, T**, **Jourdan, O**, **Jozef, G**, **King, W**, **Kirchgaessner, A**, **Klingebiel, M**, **Krassovski, M**, **Krumpen, T**, **Lampert, A**, **Landing, W**, **Laurila, T**, **Lawrence, D**, **Lonardi, M**, **Loose, B**, **Lüpkes, C**, **Maahn, M**, **Macke, A**, **Maslowski, W**, **Marsay, C**, **Maturilli, M**, **Mech, M**, **Morris, S**, **Moser, M**, **Nicolaus, M**, **Ortega, P**, **Osborn, J**, **Pätzold, F**, **Perovich, DK**, **Petäjä, T**, **Pilz, C**, **Pirazzini, R**, **Posman, K**, **Powers, H**, **Pratt, KA**, **Preußer, A**, **Quéléver, L**, **Radenz, M**, **Rabe, B**, **Rinke, A**, **Sachs, T**, **Schulz, A**, **Siebert, H**, **Silva, T**, **Solomon, A**, **Sommerfeld, A**, **Spreen, G**, **Stephens, M**, **Stohl, A**, **Svensson, G**, **Uin, J**, **Viegas, J**, **Voigt, C**, **von der Gathen, P**, **Wehner, B**, **Welker, JM**, **Wendisch, M**, **Werner, M**, **Xie, Z**, **Yue, F.** 2022. Overview of the MOSAiC expedition: Atmosphere. *Elementa: Science of the Anthropocene* **10**(1): 00060. DOI: http://doi.org/10.1525/elementa.2021.00060.

Simpson, D, **Benedictow, A**, **Berge, H**, **Bergström, R**, **Emberson, LD**, **Fagerli, H**, **Flechard, CR**, **Hayman, GD**, **Gauss, M**, **Jonson, JE**, **Jenkin, ME**, **Nyri, A**, **Richter, C**, **Semeena, VS**, **Tsyro, S**, **Tuovinen, J-P**, **Valdebenito, Á**, **Wind, P.** 2012. The EMEP MSC-W chemical transport model—Technical description. *Atmospheric Chemistry and Physics* **12**(16): 7825–7865. DOI: http://dx.doi.org/10.5194/acp-12-7825-2012.

Simpson, WR, **Alvarez-Aviles, L**, **Douglas, TA**, **Sturm, M**, **Domine, F.** 2005. Halogens in the coastal snow pack near Barrow, Alaska: Evidence for active bromine air-snow chemistry during springtime. *Geophysical Research Letters* **32**(4): L04811. DOI: http://dx.doi.org/10.1029/2004GL021748.

Simpson, WR, **von Glasow, R**, **Riedel, K**, **Anderson, P**, **Ariya, P**, **Bottenheim, J**, **Burrows, J**, **Carpenter, LJ**, **Frieß, U**, **Goodsite, ME**, **Heard, D**, **Hutterli, M**, **Jacobi, H-W**, **Kaleschke, L**, **Neff, B**, **Plane, J**, **Platt, U**, **Richter, A**, **Roscoe, H**, **Sander, R**, **Shepson, P**, **Sodeau, J**, **Steffen, A**, **Wagner, T**, **Wolff, E.** 2007. Halogens and their role in polar boundary-layer ozone depletion. *Atmospheric Chemistry and Physics* **7**(16): 4375–4418. DOI: http://dx.doi.org/10.5194/acp-7-4375-2007.

Stephenson, SR, **Wang, W**, **Zender, CS**, **Wang, H**, **Davis, SJ**, **Rasch, PJ.** 2018. Climatic responses to future trans-Arctic shipping. *Geophysical Research Letters* **45**(18): 9898–9908. DOI: http://dx.doi.org/10.1029/2018GL078969.

Sterk, HAM, **Steeneveld, G-J**, **Vihma, T**, **Anderson, PS**, **Bosveld, FC**, **Holtslag, AAM.** 2015. Clear-sky stable boundary layers with low winds over snow-covered surfaces. Part 1: WRF model evaluation. *Quarterly Journal of the Royal Meteorological Society* **141**(691): 2165–2184. DOI: http://dx.doi.org/10.1002/qj.2513.

Stroeve, J, **Notz, D.** 2018. Changing state of Arctic sea ice across all seasons. *Environmental Research Letters* **13**(10): 103001. DOI: http://dx.doi.org/10.1088/1748-9326/aade56.

Swanson, WF, **Holmes, CD**, **Simpson, WR**, **Confer, K**, **Marelle, L**, **Thomas, JL**, **Jaeglé, L**, **Alexander, B**, **Zhai, S**, **Chen, Q**, **Wang, X**, **Sherwen, T.** 2022. Comparison of model and ground observations finds snowpack and blowing snow aerosols both contribute to Arctic tropospheric reactive bromine. *Atmospheric Chemistry and Physics* **22**(22): 14467–14488. DOI: http://dx.doi.org/10.5194/acp-22-14467-2022.

Tang, G, **Zhu, X**, **Xin, J**, **Hu, B**, **Song, T**, **Sun, Y**, **Zhang, J**, **Wang, L**, **Cheng, M**, **Chao, N**, **Kong, L**, **Li, X**, **Wang, Y.** 2017. Modelling study of boundary-layer ozone over northern China—Part I: Ozone budget in summer. *Atmospheric Research* **187**: 128–137. DOI: http://dx.doi.org/10.1016/j.atmosres.2016.10.017.

Tjernström, M, **Shupe, MD**, **Brooks, IM**, **Achtert, P**, **Prytherch, J**, **Sedlar, J.** 2019. Arctic summer airmass transformation, surface inversions, and the surface energy budget. *Journal of Climate* **32**(3): 769–789. DOI: http://dx.doi.org/10.1175/JCLI-D-18-0216.1.

Tjernström, M, **Svensson, G**, **Magnusson, L**, **Brooks, IM**, **Prytherch, J**, **Vüllers, J**, **Young, G.** 2021. Central Arctic weather forecasting: Confronting the ECMWF IFS with observations from the Arctic Ocean 2018 expedition. *Quarterly Journal of the Royal Meteorological Society* **147**(735): 1278–1299. DOI: http://dx.doi.org/10.1002/qj.3971.

Toyota, K, **Dastoor, AP**, **Ryzhkov, A.** 2016. Parameterization of gaseous dry deposition in atmospheric chemistry models: Sensitivity to aerodynamic resistance formulations under statically stable conditions. *Atmospheric Environment* **147**: 409–422. DOI: http://dx.doi.org/10.1016/j.atmosenv.2016.09.055.

Toyota, K, **McConnell, JC**, **Staebler, RM**, **Dastoor, AP.** 2014. Air–snowpack exchange of bromine, ozone and mercury in the springtime Arctic simulated by the 1-D model PHANTAS—Part 1: In-snow bromine activation and its impact on ozone. *Atmospheric Chemistry and Physics* **14**(8): 4101–4133. DOI: http://dx.doi.org/10.5194/acp-14-4101-2014.

Van Dam, B, **Helmig, D**, **Doskey, PV**, **Oltmans, SJ.** 2016. Summertime surface O_3 behavior and deposition to tundra in the Alaskan Arctic. *Journal of Geophysical*

Research: Atmospheres **121**(13): 8055–8066. DOI: http://dx.doi.org/10.1002/2015JD023914.

von der Gathen, P, **Maturilli, M.** 2020. Ozone sonde profiles during MOSAiC Leg 1-2-3. DOI: http://dx.doi.org/10.1594/PANGAEA.919538.

von der Gathen, P, **Maturilli, M.** 2022. Ozone sonde profiles during MOSAiC Leg 4-5. DOI: http://dx.doi.org/10.1594/PANGAEA.941294.

Wang, C, **Graham, RM**, **Wang, K**, **Gerland, S**, **Granskog, MA.** 2019. Comparison of ERA5 and ERA-Interim near-surface air temperature, snowfall and precipitation over Arctic sea ice: Effects on sea ice thermodynamics and evolution. *The Cryosphere* **13**(6): 1661–1679. DOI: http://dx.doi.org/10.5194/tc-13-1661-2019.

Wesely, ML. 1989. Parameterization of surface resistances to gaseous dry deposition in regional-scale numerical models. *Atmospheric Environment (1967)* **23**(6): 1293–1304. DOI: http://dx.doi.org/10.1016/0004-6981(89)90153-4.

Whaley, CH, **Law, KS**, **Hjorth, JL**, **Skov, H**, **Arnold, SR**, **Langner, J**, **Pernov, JB**, **Chien, R-Y**, **Christensen, JH**, **Deushi, M**, **Dong, X**, **Faluvegi, G**, **Flanner, M**, **Fu, JS**, **Gauss, M**, **Im, U**, **Marelle, L**, **Onishi, T**, **Oshima, N**, **Plummer, DA**, **Pozzoli, L**, **Raut, J-C**, **Skeie, R**, **Thomas, MA**, **Tsigaridis, K**, **Tsyro, S**, **Turnock, ST**, **von Salzen, K**, **Tarasick, DW.** 2022. Arctic tropospheric ozone: Assessment of current knowledge and model performance. *Atmospheric Chemistry and Physics Discussions*. DOI: http://dx.doi.org/10.5194/acp-2022-319; https://acp.copernicus.org/preprints/acp-2022-319/.

Wohltmann, I, **von der Gathen, P**, **Lehmann, R**, **Maturilli, M**, **Deckelmann, H**, **Manney, GL**, **Davies, J**, **Tarasick, D**, **Jepsen, N**, **Kivi, R**, **Lyall, N**, **Rex, M.** 2020. Near-complete local reduction of Arctic stratospheric ozone by severe chemical loss in spring 2020. *Geophysical Research Letters* **47**(20): e2020GL089547. DOI: http://dx.doi.org/10.1029/2020GL089547.

Wolfe, GM, **Thornton, JA**, **McKay, M**, **Goldstein, AH.** 2011. Forest-atmosphere exchange of ozone: Sensitivity to very reactive biogenic VOC emissions and implications for in-canopy photochemistry. *Atmospheric Chemistry and Physics* **11**(15): 7875–7891. DOI: http://dx.doi.org/10.5194/acp-11-7875-2011.

Yang, X, **Blechschmidt, A-M**, **Bognar, K**, **McClure-Begley, A**, **Morris, S**, **Petropavlovskikh, I**, **Richter, A**, **Skov, H**, **Strong, K**, **Tarasick, DW**, **Uttal, T**, **Vestenius, M**, **Zhao, X.** 2020. Pan-Arctic surface ozone: Modelling vs. measurements. *Atmospheric Chemistry and Physics* **20**(24): 15937–15967. DOI: http://dx.doi.org/10.5194/acp-20-15937-2020.

Zhang, Y, **Gao, Z**, **Li, D**, **Li, Y**, **Zhang, N**, **Zhao, X**, **Chen, J.** 2014. On the computation of planetary boundary-layer height using the bulk Richardson number method. *Geoscientific Model Development* **7**(6): 2599–2611. DOI: http://dx.doi.org/10.5194/gmd-7-2599-2014.

Zhang, Y, **Seidel, DJ**, **Golaz, J-C**, **Deser, C**, **Tomas, RA.** 2011. Climatological characteristics of Arctic and Antarctic surface-based inversions. *Journal of Climate* **24**(19): 5167–5186. DOI: http://dx.doi.org/10.1175/2011JCLI4004.1.

Zhao, W, **Tang, G**, **Yu, H**, **Yang, Y**, **Wang, Y**, **Wang, L**, **An, J**, **Gao, W**, **Hu, B**, **Cheng, M**, **An, X**, **Li, X**, **Wang, Y.** 2019. Evolution of boundary layer ozone in Shijiazhuang, a suburban site on the North China Plain. *Journal of Environmental Sciences* **83**: 152–160. DOI: http://dx.doi.org/10.1016/j.jes.2019.02.016.

Zhou, J, **Cao, L**, **Li, S.** 2020. Influence of the background nitrogen oxides on the tropospheric ozone depletion events in the Arctic during springtime. *Atmosphere* **11**(4): 344. DOI: http://dx.doi.org/10.3390/atmos11040344.

Zilitinkevich, S, **Baklanov, A.** 2002. Calculation of the height of the stable boundary layer in practical applications. *Boundary-Layer Meteorology* **105**(3): 389–409. DOI: http://dx.doi.org/10.1023/A:1020376832738.

How to cite this article: Barten, JGM, Ganzeveld, LN, Steeneveld, G-J, Blomquist, BW, Angot, H, Archer, SD, Bariteau, L, Beck, I, Boyer, M, von der Gathen, P, Helmig, D, Howard, D, Hueber, J, Jacobi, H-W, Jokinen, T, Laurila, T, Posman, KM, Quéléver, L, Schmale, J, Shupe, MD, Krol, MC. 2023. Low ozone dry deposition rates to sea ice during the MOSAiC field campaign: Implications for the Arctic boundary layer ozone budget. *Elementa: Science of the Anthropocene* 11(1). DOI: https://doi.org/10.1525/elementa.2022.00086

Domain Editor-in-Chief: Jody W. Deming, University of Washington, Seattle, WA, USA

Associate Editor: Lisa A. Miller, Institute of Ocean Sciences, Fisheries and Oceans Canada, Sidney, Canada

Knowledge Domain: Ocean Science

Part of an Elementa Special Feature: The Multidisciplinary Drifting Observatory for the Study of Arctic Climate (MOSAiC)

Published: February 15, 2023 **Accepted:** January 4, 2023 **Submitted:** June 17, 2022

ELEMENTA Science of the Anthropocene

Elem Sci Anth is a peer-reviewed open access journal published by University of California Press.

OPEN ACCESS